

# Kilometer-scale autonomous navigation in subarctic forests: challenges and lessons learned

---

**Dominic Baril\***

Norlab, Université Laval  
 Québec, QC, Canada G1V 0A6  
 dominic.baril@norlab.ulaval.ca

**Simon-Pierre Deschênes**

Norlab, Université Laval  
 Québec, QC, Canada G1V 0A6

**Olivier Gamache**

Norlab, Université Laval  
 Québec, QC, Canada G1V 0A6

**Maxime Vaidis**

Norlab, Université Laval  
 Québec, QC, Canada G1V 0A6

**Damien LaRocque**

Norlab, Université Laval  
 Québec, QC, Canada G1V 0A6

**Johann Laconte**

Norlab, Université Laval  
 Québec, QC, Canada G1V 0A6

**Vladimír Kubelka**

Norlab, Université Laval  
 Québec, QC, Canada G1V 0A6

**Philippe Giguère**

Norlab, Université Laval  
 Québec, QC, Canada G1V 0A6

**François Pomerleau**

Norlab, Université Laval  
 Québec, QC, Canada G1V 0A6  
 francois.pomerleau@norlab.ulaval.ca

## Abstract

Challenges inherent to autonomous wintertime navigation in forests include lack of reliable a Global Navigation Satellite System (GNSS) signal, low feature contrast, high illumination variations and changing environment. This type of off-road environment is an extreme case of situations autonomous cars could encounter in northern regions. Thus, it is important to understand the impact of this harsh environment on autonomous navigation systems. To this end, we present a field report analyzing teach-and-repeat navigation in a subarctic region while subject to large variations of meteorological conditions. First, we describe the system, which relies on point cloud registration to localize a mobile robot through a boreal forest, while simultaneously building a map. We experimentally evaluate this system in over 18.6 km of autonomous navigation in the teach-and-repeat mode. We show that dense vegetation perturbs the GNSS signal, rendering it unsuitable for navigation in forest trails. Furthermore, we highlight the increased uncertainty related to localizing using point cloud registration in forest corridors. We demonstrate that it is not snow precipitation, but snow accumulation that affects our system's ability to localize within the environment. Finally, we expose some lessons learned and challenges from our field campaign to support better experimental work in winter conditions.

---

\*Direct correspondence to: Dominic Baril, email: dominic.baril@norlab.ulaval.ca

# 1 Introduction

Autonomous navigation has enabled mobile robots to be deployed in a wide variety of areas in order to support human operation. Specific examples include forestry (Oliveira et al., 2021), mining (J. A. Marshall et al., 2016), disaster search and rescue (Kruijff et al., 2014), and military applications (Simon, 2015). Recently, Van Brummelen et al. (2018) have released a comprehensive review of the state-of-the-art perception technologies for autonomous vehicles. In this review, the authors identified key future challenges that need to be addressed for safer systems. One of these challenges is increasing the reliability of Simultaneous Localization and Mapping (SLAM) algorithms to external factors, such as dynamic environments, poor lighting, and weather conditions. In this regard, enabling true long-term autonomy for mobile robots will eventually require systems to be resilient to any road and weather condition.

To progress towards solving the challenges mentioned by Van Brummelen et al. (2018), this research study aims to examine the impact of northern environment and weather on the state-of-the-art autonomous navigation approaches. Access to the Montmorency boreal forest, located 70 km North of Québec City, Canada, during winter enabled us to deploy an autonomous system in difficult meteorological conditions, which allowed us to conduct this study. Thus, we present a field report on the deployment of an autonomous navigation framework in a boreal forest under harsh winter conditions. Subarctic regions are mostly covered by the boreal forest biome, and are thus ideal for this study. Boreal forests are characterized by dense, closed-crown conifer vegetation (Russell & Ritchie, 1988) and harsh winter weather. In the forest, we distinguish two path types: forest roads and forest trails, both shown in Figure 1. Forest roads are built to accommodate various vehicles, while forest trails are narrow and are not built to accommodate typical road vehicles. The dense vegetation surrounding forest trails is not traversable by most unmanned ground vehicles (UGVs), and thus autonomous navigation error tolerance is low when navigating on these trails. Moreover, dense vegetation is known to cause problems for autonomous navigation due to interference of the canopy with the Global Navigation Satellite System (GNSS) signal (Kubelka et al., 2020). In addition to explaining the path types, Figure 1 also demonstrates the meteorological conditions of this field deployment. It was conducted on 0.7 m compacted snow cover, with precipitation and in sub-zero temperatures. These conditions complicate the logistics of the deployment, diminish the endurance both of the robotic system and the personnel, and require punctual planning. Yet, they reveal weaknesses of the contemporary robotic technology and point to new research problems. This field report goes beyond prior work that identified snow-covered terrain as impracticable for vision-based SLAM (Paton et al., 2017).

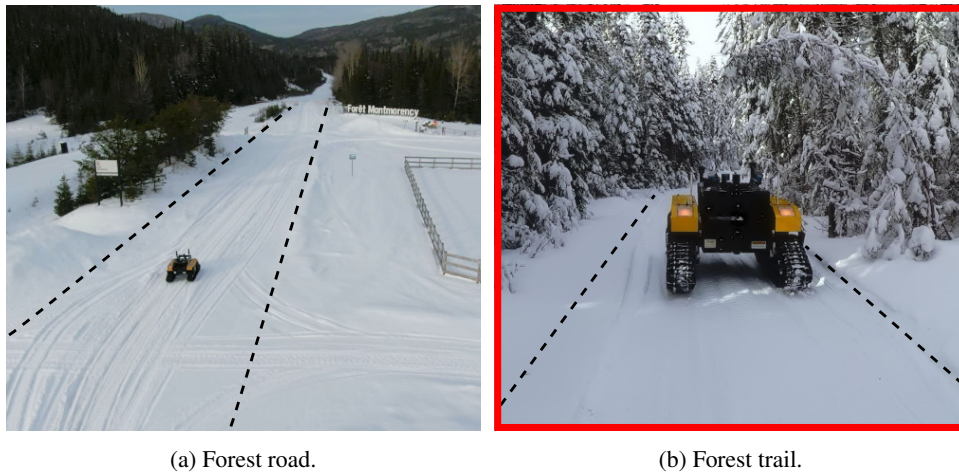


Figure 1: The main focus of this work is evaluating the impact of biome and weather on autonomous navigation. We distinguish two distinct path types, namely forest roads and forest trails. (a): The system navigating on a wide forest path, allowing greater system inaccuracies. (b): A forest trail, where the dense vegetation prevents the robot from navigating outside the trail and blocks the GNSS signal. The error tolerance for forest trail navigation is much lower than for forest roads. In this work, the majority of autonomous navigation is conducted in forest trails, as highlighted by the red mark on the right picture.

To generate observations on the impact of northern environments on autonomous navigation technologies, we have built the Weather-Invariant Lidar-based Navigation (WILN) system. The WILN framework relies primarily on lidar sensor range measurements and point cloud registration for localization. Lidar sensors are ideal for wintertime navigation in a boreal forest since their active nature makes them independent of scene illumination, as demonstrated by Krüsi et al. (2015). Generally, teach-and-repeat frameworks follow the principle of a mobile robot repeating previously demonstrated paths. In this work, we use data gathered during three distinct manual traversals on forest roads and trails to repeat them multiple times throughout an entire week in changing meteorological and illumination conditions.

The specific contributions of this paper are: (i) a comprehensive study of the impact of the boreal forest biome on lidar- and GNSS-based localization and autonomous navigation; (ii) an overview of the impact of snow accumulation on the reliability of lidar-based localization over multiple days; and (iii) a description of the WILN system, designed to enable wintertime autonomous navigation in a boreal forest. The remainder of this paper is organized as follows: [Section 2](#) overviews the related work and robotic deployments performed in winter weather conditions. It also compares related GNSS-denied long-range autonomous navigation algorithms. [Section 3](#) describes the WILN framework in detail, including both our localization pipeline and the path-following controller. [Section 4](#) describes the environment in which we conducted our deployments and presents the system hardware and the implementation parameters of the WILN framework. [Section 5](#) provides the results of the field trials and [Section 6](#) discusses them in the context of the forest and subarctic conditions. It further presents the lessons learned during this deployment. Finally, we conclude this paper in [Section 7](#).

## 2 Related work

The aim of this paper is to present the impact of the boreal forest and winter conditions on autonomous navigation technologies with the goal of enabling true long-term robot autonomy. In this section, we show that while various off-road robotic deployments in winter conditions are documented in the literature, they mostly rely on the GNSS signal for localization (Lever et al., 2013). Vision-based localization approaches have enabled autonomous navigation in GNSS-denied environments. However, winter conditions have been shown to severely affect the performance of such approaches (Paton et al., 2017). Wintertime autonomous navigation in a boreal forest requires localization capabilities that are resilient to both winter conditions and GNSS-denied environments. Active sensors such as lidars are ideal for solving this problem since they are robust to lighting variation (Krüsi et al., 2015).

GNSS-based localization has been the standard for autonomous navigation in polar environments. The first rover to have been deployed in polar regions is *Nomad*, a gasoline-powered UGV weighing 725 kg. *Nomad* was stationed at Elephant Moraine, Antarctica for a duration of four weeks with the goal of autonomously identifying meteorites (Apostolopoulos et al., 2000). The robot reached speeds upwards of 0.5 m/s while using differential-GNSS as the primary method of localization. The platform also used the stereo cameras and the lidar sensor for obstacle detection. However, stereo vision was found to be ineffective on blue ice and snow in Antarctica due to extreme lack of texture (Moorehead et al., 1999). Additionally, several operators were required in order to manually avoid undetected rocks. Expanding on this work, *MARVIN I* and *MARVIN II* were two diesel-powered Skid-steering mobile robots (SSMRs) weighing 720 kg. *MARVIN I* and *MARVIN II* were deployed in Greenland (Stansbury et al., 2004) and Antarctica (Gifford et al., 2009) respectively. The goal of these robots was to increase survey safety in remote polar regions. The requirement of heavy sensor payloads led to the selection of large vehicles. *MARVIN I* used again Real-time Kinematics (RTK) GNSS as the primary method of localization, achieving a centimeter-level accuracy in open environments. *MARVIN II* did not rely on RTK GNSS radio signal loss when navigating out of the RTK reference receiver range. Transfer from RTK to differential-GNSS increased rover oscillation with respect to the reference path. Through the *MARVIN I* and *II* deployments, Stansbury et al. (2004) highlighted the fact that turning maneuvers with SSMRs were linked to a high risk of immobilization in deep snow. Later, *Yeti*, a battery-powered 81 kg UGV was deployed to conduct Ground Penetrating Radar surveys in order to detect subsurface crevasses or other voids. Knowledge about such crevasses would enable human operators to plan safer paths for larger vehicles. *Yeti* did not include any obstacle detection system. During surveys, *Yeti* reached a top speed of  $2.2 \text{ m s}^{-1}$  and managed to acquire data on hundreds of crevasse encounters. It even located a previously undetected buried building in the South Pole. The aforementioned work on field robotics in polar regions allowed the identification of various issues related to autonomous navigation on snow-covered terrain.

Due to the complex nature of localizing in polar regions, GNSS is the most popular means of localization for such regions. However, one should also note that the state-of-the-art in mobile robots' perception has considerably evolved in the years that passed since the last field report was conducted in polar regions.

Since the GNSS signal is not always reliable due to the multipath effect or signal absorption due to tree canopy (Kubelka et al., 2020), approaches independent to these effects have been proposed. Furgale and Barfoot (2010) were the first to show that Visual Teach and Repeat (VT&R) approaches are robust enough to perform large-scale autonomous navigation in GNSS-denied environments. The authors have deployed their system in the Canadian High Arctic. This environment was selected because of its similarity to lunar and martian terrain. Most features consisted of rocks located within the reference trajectory. In this work, they successfully repeated reference paths up to ten hours after they were manually driven. However, sensitivity to illumination change was identified as the main limit of the system. Thus, Churchill and Newman (2013) later introduced *Experience-based navigation* to increase the robustness of VT&R to scene appearance change, caused by illumination variation or dynamic environment changes. This feature was added in VT&R through *Multi-experience Localization*, with the added ability to use landmarks from previous experiences in the same localization problem (Paton et al., 2016). In this work, the authors extend the allowable time between teach and repeat runs from a few hours to multiple days. Paton et al. (2015) also added color-constant image transformations to VT&R to mitigate the impact of illumination variations. Color-constant image transformations have been used by Clement et al. (2017) to perform autonomous route repeating by using the VT&R framework while relying solely on a monocular camera. While vision-based localization was demonstrated to be robust to illumination variation, Paton et al. (2015) have observed that localization frameworks relying only on passive cameras fail to localize in dark conditions.

To enable nighttime vision-based navigation, McManus et al. (2013) have proposed to use an intensity-based lidar to replace cameras for the VT&R framework. While this work demonstrates that this system is resilient to low illumination conditions, it suffers from motion distortion issues. Using headlights, MacTavish et al. (2017) proposed a bag-of-words approach to prioritize experiences most relevant to live operation. This in turn allows a growing number of robot experiences while limiting computation requirements. In this work, the authors have successfully repeated paths over a 31 h period, including day and night driving relying on headlights. Extending the experimental evaluation of VT&R, Paton et al. (2018) have logged over 140 km of autonomous navigation in an untended gravel pit, also including nighttime navigation. Clement et al. (2020) have used a deep neural network to learn a nonlinear color transform mapping that maximizes vision-based localization resiliency to appearance change. In this work, they successfully localized on routes over a 30 h period by relying only on a single experience. However, Congram and Barfoot (2021) still observed vision-based localization failures in low illumination, even when using headlights. In this work, the authors proposed to fuse vision-based localization with GNSS measurements to enable VT&R systems to function in areas where vision localization fails.

Vision-based localization was tested on snow-covered terrain numerous times. *Sno-mote Mk1* and *Mk2* were deployed on Alaskan glaciers and Wapekoneta, Ohio (Williams & Howard, 2009). *Sno-motes* are dual-drive 1:10 scale snowmobiles equipped with a single camera and GNSS. These robots were used to conduct manually-driven traverses of about 100 m at a speed of  $1 \text{ m s}^{-1}$ . The data gathered with the *Sno-motes* was then used to enhance visual SLAM feature extraction methods in snow. Despite improving feature detection methods on snow, it was shown that snow is still feature-sparse (Williams & Howard, 2009). Paton et al. (2017) then showed that vision-based localization is robust to intra-seasonal, daily scene appearance change, by successfully repeating more than 26 km over multiple days. In this work, VT&R was also deployed on a 250 m path featuring a 0.3 cm snow cover. However, deep snow path-following leads to unstable UGV behavior due to features almost only being observed on the horizon, leading to inaccurate pose estimates, which led to path-following instability. Active sensors have the potential to be resilient to the issues encountered by vision-based localization due to their independence from scene illumination and lack of feature contrast (e.g., when navigating on snow-covered terrain).

On the other hand, lidar-based localization is resilient to illumination variation, which can lead to localization failure for vision-based systems. J. Marshall et al. (2008) were the first to suggest a Lidar Teach and Repeat (LT&R) using encoders and 2D lidars. In this work, a sequence of locally consistent and overlapping topometric maps (i.e., occupancy grids) are recorded along the path using 2D lidar measurements to allow the robot to localize during the repeat phase. The system was proven efficient for repeating paths in underground tunnels on a 10 t capacity hauler. Still



relying only on 2D lidar scans for localization, Sprunk et al. (2013) have proposed to localize directly on 2D lidar scans, removing the requirement to build a topometric map offline. This system was deployed in an indoor, structured environment, resulting in a millimetric localization accuracy. Later, Mazuran et al. (2015) improved this framework by introducing a trajectory optimization step between the teach and the repeat phase, while still deploying the system in a similar indoor environment.

More related to off-road environments, Nieto et al. (2003) have proposed the FastSLAM algorithm relying on 2D lidar scans, which they have tested on the Victoria Park dataset. This dataset was recorded within an urban park, on uneven terrain and through sparse vegetation. In this work, the various trees in the park were used as landmarks to localize with the FastSLAM algorithm. Later, Jagbrant et al. (2015) have deployed a similar lidar-based localization system in an almond orchard. However, an almond tree orchard contains significantly sparser vegetation than the boreal forest. Zhang and Singh (2018) have deployed a lidar and inertial measurement unit (IMU)-based framework in a sparse forest environment. In this work, they have shown resilience to multi-seasonal change by merging a summer and winter map. However, due to the location where this work was conducted, no analysis of the impact of snowfall is discussed. Recently, Ren et al. (2021) have deployed a lidar localization system in a desert biome. They identified the lack of features and geometrical constraints as an issue for point cloud registration. This issue is similar to the low feature contrast problem that affects vision-based approaches in snow-covered terrain (Paton et al., 2017).

Relying on the iterative closest point (ICP) algorithm, Krüsi et al. (2015) have deployed a LT&R system in off-road environments and busy city streets, successfully repeating paths of up to 1.3 km. These deployments have shown the resiliency of lidar-based perception to off-road and urban environments, under high illumination variations. However, this deployment does not cover the impact of dense vegetation and snowfall. In previous work, we have shown that using the ICP algorithm to register 3D lidar scans, we can produce large-scale maps of a boreal forest offline (Babin et al., 2019). This paper aims to describe the field deployment of the WILN framework in a boreal forest during five days, effectively subjecting it to weak GNSS signal, high illumination variations and low feature contrast. Such deployment conditions combine the challenges of navigation in snow-covered and GNSS-denied, constrained environments. We report the impact of dense vegetation in forest trails and of snow accumulation on the performance of the WILN system.

### 3 Weather-Invariant Lidar-based Navigation (WILN) system description

WILN is an autonomous teach-and-repeat framework designed to be robust to kilometer-scale navigation, severe weather and GNSS-denied conditions. As a localization prior, the system relies on IMU measurements and the wheel odometry, as described in Section 3.1. Registering 3D lidar scans through the ICP algorithm is the primary means of localization (Section 3.2). Map maintenance and tiling modules were added to enable kilometer-scale SLAM, both of which are described in Section 3.3. As for most teach-and-repeat frameworks, two modes are defined: the *teach phase* and the *repeat phase* (Section 3.4). A kinematic controller was selected to compute appropriate commands to solve the path-following problem (Section 3.5). This section will end with a visual representation of all WILN system components and their interactions.

Four coordinate frames are defined in the WILN framework, as illustrated in Figure 2. First, the global map frame  $\mathcal{G}$  is defined, representing the world the robot navigates in. Second, the robot frame  $\mathcal{R}$  is defined with its origin in the base of the robot chassis. The  $x$ -axis of the robot frame  $\mathcal{R}$  is parallel to the longitudinal direction and the  $y$ -axis is parallel to the lateral direction of the robot. Thirdly, the lidar frame  $\mathcal{L}$  coincides with the lidar sensor origin. The rigid transform from the robot frame to the lidar frame  ${}^{\mathcal{L}}_{\mathcal{R}}T$  is assumed to be constant and found through system calibration. The reading point clouds (i.e., input points)  $\mathcal{P}$  are originally observed in the lidar frame  $\mathcal{L}$  and the reference point clouds (i.e., map points) are expressed in the map frame  $\mathcal{G}$ . The transform  ${}^{\mathcal{G}}_{\mathcal{R}}T$  between the frames  $\mathcal{R}$  and  $\mathcal{G}$  is updated by the ICP algorithm and constitutes the robot localization. For the path-following algorithm running in the repeat phase, the Frenet-Serret frame  $\mathcal{S}$  is defined directly on the path. Lastly, the reference trajectory recorded in the teach phase is expressed as a vector of consecutive robot poses  $x_{\text{ref}} = \{{}^{\mathcal{G}}_{\mathcal{R}}T_1, {}^{\mathcal{G}}_{\mathcal{R}}T_2, \dots, {}^{\mathcal{G}}_{\mathcal{R}}T_n\}$ , where  $n$  is the number of recorded poses in the trajectory.

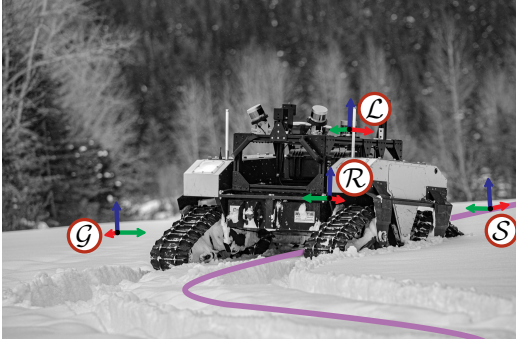


Figure 2: Coordinate frames used for WILN. In this instance, the robot is moving towards the path frame  $\mathcal{S}$ . The reference path that the robot aims to follow is drawn in light purple. The remaining relevant coordinate frames are the map frame  $\mathcal{G}$ , the lidar frame  $\mathcal{L}$  and the robot frame  $\mathcal{R}$ .

### 3.1 Localization prior: IMU and wheel odometry

The ICP algorithm requires high-frequency prior estimates of  ${}^{\mathcal{G}}_{\mathcal{L}}\tilde{\mathbf{T}}$  that capture the motion between every two consecutive lidar scans. In WILN, the prior  ${}^{\mathcal{G}}_{\mathcal{L}}\tilde{\mathbf{T}}$  is estimated through IMU measurements and wheel odometry. The robot orientation is estimated using the Madgwick filter<sup>1</sup> (Madgwick et al., 2011) based on gyroscope and accelerometer measurements. Linear displacement is based on wheel odometry, while taking into account the estimated robot orientation. The prior  ${}^{\mathcal{G}}_{\mathcal{L}}\tilde{\mathbf{T}}$  is generated synchronously with the IMU at a frequency of 100 Hz. When subject to motion, it should be noted that lidar sensors generate skewed reading point clouds  ${}^{\mathcal{L}}\mathcal{P}_s$ . Hence, we deploy a point cloud de-skewing filter in our system. First proposed by Bosse and Zlot (2009), such algorithms correct point cloud distortions by taking the lidar intra-scan motion into account. Following the same idea, our high-frequency  ${}^{\mathcal{G}}_{\mathcal{L}}\tilde{\mathbf{T}}$  prior is used to de-skew the raw input point cloud. The resulting corrected  ${}^{\mathcal{L}}\mathcal{P}$  is the one used in the ICP algorithm.

### 3.2 Iterative closest point (ICP)

To localize the robot, the incoming de-skewed reading point clouds  ${}^{\mathcal{L}}\mathcal{P}$  are registered to the reference point cloud  ${}^{\mathcal{G}}\mathcal{Q}$  using the ICP algorithm. This allows a map of the environment to be built during the teach phase and enables the robot to be localized in this map during the repeat phase. An overview of the ICP pipeline is shown in Figure 3. The ICP algorithm iteratively matches points between two point clouds and looks for a rigid transform that minimizes the distance between each pair of the matched points. Pomerleau et al. (2015) presented a comprehensive review of the state-of-the-art for the ICP algorithm. The WILN registration component is based on the modules presented in this review. To increase robustness of the algorithm, we apply the following three input filters to the reading  ${}^{\mathcal{L}}\mathcal{P}$  before registering it into the reference  ${}^{\mathcal{G}}\mathcal{Q}$ :

1. **Random sub-sampling filter** parameterized by the ratio  $\eta_s \in [0, 1]$  of the points kept after the sub-sampling. This sub-sampling is critical to reducing the computation time of the ICP algorithm to allow the SLAM problem to be solved in real time (Pomerleau et al., 2011).
2. **Bounding box filter** parameterized by the bounding box coordinates  $\mathbf{b}_i = (x_{\min}, x_{\max}, y_{\min}, y_{\max}, z_{\min}, z_{\max}) \in \mathbb{R}^6$ . It removes points originating from the robot body that would otherwise cause a trail of points in the reference point cloud  $\mathcal{Q}$ .
3. **Radius filter** parameterized by the maximum radius  $r$  around the lidar. Beyond this radius, the reading points are discarded. This allows only the relevant vicinity around the robot to be considered to further reduce the computation time.

In our implementation,  ${}^{\mathcal{L}}\mathcal{P}$  is observed in the lidar frame  $\mathcal{L}$  and  ${}^{\mathcal{G}}\mathcal{Q}$  is defined in the map frame  $\mathcal{G}$ . Thus, the ICP algorithm estimates the transform  ${}^{\mathcal{G}}_{\mathcal{L}}\hat{\mathbf{T}}$  by minimizing an error function  $e$  using

$${}^{\mathcal{G}}_{\mathcal{L}}\hat{\mathbf{T}} = \arg \min_{\mathbf{T}} [e({}^{\mathcal{G}}\mathcal{P}, {}^{\mathcal{G}}\mathcal{Q})], \quad (1)$$

<sup>1</sup>[https://github.com/bjohnsonfl/Madgwick\\_Filter](https://github.com/bjohnsonfl/Madgwick_Filter)

where  ${}^{\mathcal{G}}\mathcal{P}$  is the reading point cloud  $\mathcal{P}$  expressed in the map frame  $\mathcal{G}$ . For the first iteration, the prior  ${}^{\mathcal{G}}_{\mathcal{L}}\tilde{\mathbf{T}}$  is used to compute this rigid transformation. The prior computation is explained in [Section 3.1](#). To compute the error function, we associate points between the reading point cloud and the reference point cloud. Following this step, the ICP algorithm computes the optimal transform by iteratively minimizing the error between  ${}^{\mathcal{G}}\mathcal{P}$  and  ${}^{\mathcal{G}}\mathcal{Q}$ , as specified in [Equation 1](#). For better clarity, the remainder of these sections concentrates on a single ICP iteration step that would be repeated until convergence.

Point matching is first done by finding the closest points in  ${}^{\mathcal{G}}\mathcal{Q}$  for each point of  ${}^{\mathcal{G}}\mathcal{P}'$ . Thus, multiple points of  ${}^{\mathcal{G}}\mathcal{Q}$  can be associated with each point of  ${}^{\mathcal{G}}\mathcal{P}'$ . Nearest neighbor search is carried out via the use of a kd-tree<sup>5</sup> to decrease computation time. The matcher is parameterized by the number of nearest neighbors for each  $\mathcal{P}$  point  $n_m \in \mathbb{Z}_{>0}$  and the maximum allowable distance for a match  $d_{\max} \in \mathbb{R}_{>0}$ . In order to speed up the nearest neighbor searches, the  $\varepsilon \in \mathbb{R}_{>0}$  parameter is set to 1 to allow approximations, as described in (Arya & Mount, 1993). Subsequently, we apply an outlier filter to add binary weights to each matched point to remove the outlier matches from the error function. The outlier filter adds a positive binary weight to the  $\eta_d \in [0, 1]$  proportion of nearest matches. Formally, let  $\mathcal{M}_{\text{all}} = \text{match}(\mathcal{P}, \mathcal{Q}) = \{(\mathbf{p}, \mathbf{q}) \in \mathcal{P} \times \mathcal{Q}\}$  be the set of matches between  $\mathcal{P}$  and  $\mathcal{Q}$ . We also define  $\mathcal{M} \subseteq \mathcal{M}_{\text{all}}$ , which contains only the  $n_m$  closest pairs of  $\mathcal{M}$  for each point of  $\mathcal{P}$  with a euclidean distance below  $d_{\max}$ . Let  $\mathcal{W} = \text{outlier}(\mathcal{P}, \mathcal{Q}) = \{w(\mathbf{p}, \mathbf{q}) : (\mathbf{p}, \mathbf{q}) \in \mathcal{M}\}$  be the weights associated with these matches. Our system uses the point-to-plane error function, defined by

$$e(\mathcal{P}, \mathcal{Q}) = \sum_{k=1}^K w(\mathbf{p}_k, \mathbf{q}_k) \left\| (\mathbf{p}_k - \mathbf{q}_k) \cdot \mathbf{n}_k \right\|_2, \quad (2)$$

where  $K$  is the number of matches in  $\mathcal{M}$  and  $\|\cdot\|_2$  is the L2 norm. The normal vector  $\mathbf{n}_k$  around the 3D point  $\mathbf{q}_k$  in  $\mathcal{Q}$  is computed prior to the ICP algorithm. The error in [Equation 2](#) can be iteratively minimized by recomputing the set of matched points  $\mathcal{M}$  and their associated weights  $w$  at each iteration. Moreover, in the minimization process, we only optimize the translation and the yaw rotation, assuming that the prior roll and pitch angles are already optimal. This holds in the case of precise IMU calibration w.r.t the robot frame  $\mathcal{R}$ . Transformation checkers are added to WILN to detect erroneous ICP solutions. An error is raised if the prior error exceeds predefined thresholds in translation error  $\varepsilon_{t_{\min}} \in \mathbb{R}_{>0}$  or angular error  $\varepsilon_{\theta_{\min}} \in \mathbb{R}_{>0}$ . Additionally, the iterative process of the ICP algorithm is stopped after a maximum number of iterations  $i_{\max} \in \mathbb{Z}_{>0}$  is reached, returning the last transform. The resulting transform  ${}^{\mathcal{G}}_{\mathcal{L}}\hat{\mathbf{T}}$  can be used to express the 3D robot pose in  $\mathcal{G}$  by chaining  ${}^{\mathcal{G}}_{\mathcal{L}}\hat{\mathbf{T}} {}^{\mathcal{L}}_{\mathcal{R}}\mathbf{T}$  since the latter was evaluated through system calibration. The ICP algorithm also returns the reading point cloud in the map frame  ${}^{\mathcal{G}}\mathcal{P}$ . Our implementation is strongly based on the `libpointmatcher` library (Pomerleau et al., 2013).<sup>2</sup> This library allows fast registration of large point clouds, which is essential to solving the SLAM problem in real time.

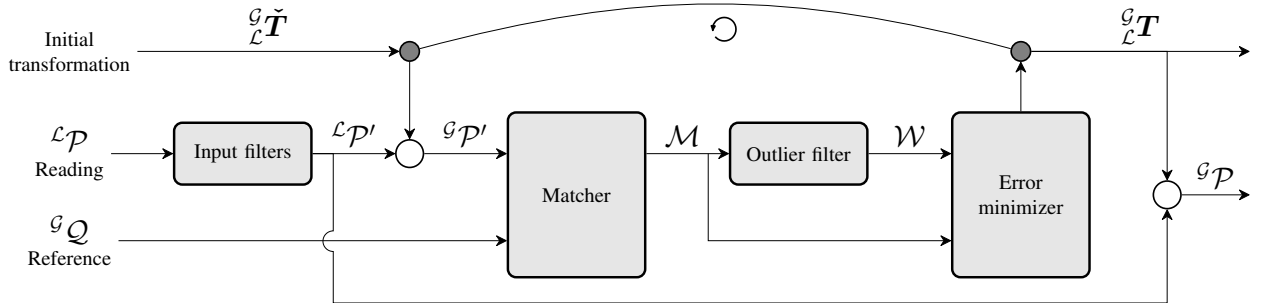


Figure 3: The ICP pipeline. The reading point cloud  ${}^{\mathcal{L}}\mathcal{P}$  is filtered, and the initial transformation  ${}^{\mathcal{G}}_{\mathcal{L}}\tilde{\mathbf{T}}$  is applied to it. The matcher finds sets of neighbors in  ${}^{\mathcal{G}}\mathcal{Q}$  for each point of  ${}^{\mathcal{G}}\mathcal{P}'$ , which compose the set of matches  $\mathcal{M}$ . An outlier filter is then used to compute weights  $w$  associated with the matches  $\mathcal{M}$ . The weights  $w$  and the matches  $\mathcal{M}$  are then used in the error minimizer to compute an output transformation  ${}^{\mathcal{G}}_{\mathcal{L}}\hat{\mathbf{T}}$ . The matching, outlier filtering and error minimization steps are done iteratively until the error is beneath the settled threshold.

<sup>2</sup><https://github.com/ethz-asl/libpointmatcher>

### 3.3 Large-scale mapping

The large-scale mapping sub-system uses the ICP implementation described in [Section 3.2](#) to solve the SLAM problem in large-scale navigation. At each time step, a lidar scan  ${}^{\mathcal{L}}\mathcal{P}$  is measured and registered to the reference map  ${}^{\mathcal{G}}\mathcal{Q}$ , yielding the transformed and filtered reading  ${}^{\mathcal{G}}\mathcal{P}$  and the estimated transform between the lidar and map frames  ${}^{\mathcal{G}}\hat{T}$ . The registered scan  ${}^{\mathcal{G}}\mathcal{P}$  is appended to the reference point cloud  ${}^{\mathcal{G}}\mathcal{Q}$ . To maintain a point density in the map, a point is only appended if its distance to the closest point in the map exceeds the user-defined minimal threshold  $\rho \in \mathbb{R}_{>0}$ . After merging the input point cloud into the map, two post-filters are applied to the map:

1. **Surface normal filter** computes the surface normals for all points required by the point-to-plane minimization described in [Equation 2](#). For each map point, the positions of the  $n_n \in \mathbb{Z}_{>0}$  closest points are taken into account to estimate the local surface normal.
2. **Dynamic point filter** removes points that are identified as dynamic, originating from, e.g., walking pedestrians, falling snow, etc. Its implementation is based on the one proposed by Pomerleau et al. (2014). The dynamic filter allows dynamic elements to be removed from the map, allowing the map to be maintained extended periods of time. To filter out the dynamic points, ray tracing is used. If an incoming scan  ${}^{\mathcal{L}}\mathcal{P}$  point is located behind a map point  ${}^{\mathcal{L}}\mathcal{Q}$ , the probability of this map point being dynamic is increased. If this probability surpasses the predefined threshold  $\tau_d \in [0, 1]$ , it is effectively removed from  ${}^{\mathcal{G}}\mathcal{Q}$ . To limit computation time for this filter, map points located further than the sensor range  $r$  do not enter the filtering process.

This new map  ${}^{\mathcal{G}}\mathcal{Q}'$  is sent to the *voxel manager* module, illustrated in [Figure 4](#). The purpose of the *voxel manager* is to limit the computational complexity of the map maintenance, instead of letting it grow with its size. Our implementation of the *voxel manager* module is similar to the one proposed by Ren et al. (2021). It involves the following steps: the new map  ${}^{\mathcal{G}}\mathcal{Q}'$  is divided into voxels and only the voxels that are close to the robot are kept in the Random Access Memory (RAM). All points located within those voxels are considered to be the local map  ${}^{\mathcal{G}}\mathcal{Q}$ . The remaining voxels represent the non-local map  ${}^{\mathcal{G}}\mathcal{Q}_{\text{DB}}$  and are stored in the database on the system hard drive.

The local map  ${}^{\mathcal{G}}\mathcal{Q}$  voxels constitute a cube following the position of the  $\mathcal{L}$  frame. The center of this cube is maintained close to the origin of the  $\mathcal{L}$  frame. The initial length of its edge is defined as twice the lidar sensor range  $r$  plus a margin of two voxels on each side. This margin gives the manager enough time to load and unload voxels as the robot moves through the map. The loading and unloading operations are triggered each time the robot crosses two distinct voxel borders, preventing unnecessary computations if the robot oscillates on a single voxel border. The side effect is the varying number of voxels in the local map  ${}^{\mathcal{G}}\mathcal{Q}$ , as can be observed in the example for the second robot pose  $\mathcal{R}_{t_2}$  in [Figure 4](#). In this case, tile loading will be triggered once the sensor range crosses the next voxel frontier, which explains why only one voxel separates the sensor range from the local map edge. The *voxel manager* allows the maximum map maintenance computation time to be limited, allowing the system to solve the SLAM problem for kilometer-scale environments. This module is parametrized by the voxel size  $v_s \in \mathbb{R}_{>0}$ , in meters.

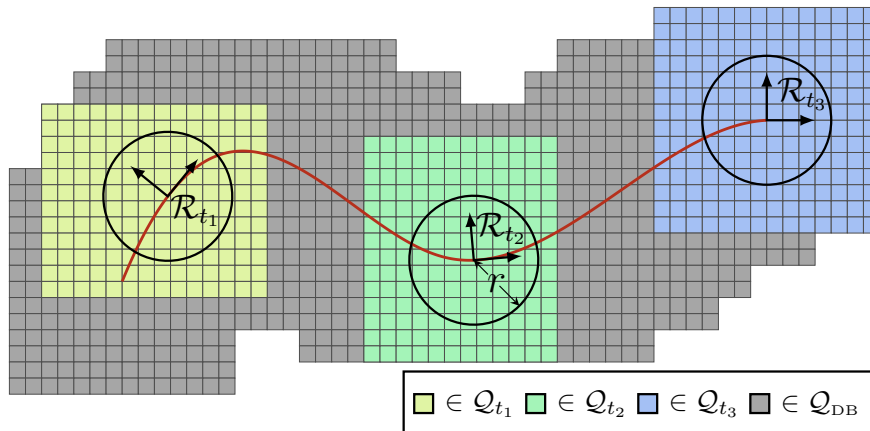


Figure 4: The management of the map by the *voxel manager* module. The robot trajectory is represented by the red line. Three distinct robot poses are represented by  $\mathcal{R}_{t_1}$ ,  $\mathcal{R}_{t_2}$  and  $\mathcal{R}_{t_3}$ . The local map  ${}^{\mathcal{G}}\mathcal{Q}$  voxels are represented by the light yellow, green and blue colors and the non-local map  ${}^{\mathcal{G}}\mathcal{Q}_{\text{DB}}$  voxels by the dark gray color.

### 3.4 Teach and repeat phases

During the teach phase, the robot is driven along a specific path by a human operator. The large-scale mapping framework presented in [Section 3.3](#) is used to build the reference map. The local  ${}^{\mathcal{G}}Q$  and non-local  ${}^{\mathcal{G}}Q_{DB}$  map voxels introduced in [Section 3.3](#) are saved to a map database. The sequence of robot poses  $\mathbf{x}_{ref}$  estimated by the ICP algorithm is sub-sampled to keep only points that are at least  $d_{ref}$  apart from each other. This sub-sampled trajectory is also saved in the database and constitutes the reference path  $\mathbf{x}_{ref}$  for the repeat phase. The system can be taught various reference trajectories and maps, all of which are stored on the robot's hard drive.

During the repeat phase, the complete reference map and the reference path  $\mathbf{x}_{ref}$  are first loaded from the database. The *voxel manager* then re-builds the local map  ${}^{\mathcal{G}}Q$  and the non-local map  ${}^{\mathcal{G}}Q_{DB}$  voxels according to the robot's position. In this phase, no points are appended to the reference map and the ICP algorithm is only used to localize the robot in the local map. The estimated pose of the robot  ${}^{\mathcal{G}}_{\mathcal{R}}\hat{T}$  is then projected as a planar pose  $\mathbf{x}_{2D}$  and used by the path-following algorithm described in the next section. The path-following algorithm computes the output system commands  $\mathbf{u}$  to steer the UGV along the  $\mathbf{x}_{ref}$  poses.

### 3.5 Path-following

Once the robot's pose  ${}^{\mathcal{G}}_{\mathcal{R}}\hat{T}$  has been estimated and the reference trajectory  $\mathbf{x}_{ref}$  loaded from the database, this information is used as the input to the path-following controller. The output of the path-following algorithm are the commanded longitudinal and angular velocities, respectively defined in the vector  $\mathbf{u} = [v_x, \omega] \in \mathbb{R}^2$ . The WILN framework uses the Orthogonal-Exponential (OE) controller to compute the command vector  $\mathbf{u}$ . This controller computes angular velocity through the orthogonal projection of the robot pose on the reference path and various heuristics to compute linear velocity (Huskić et al., 2017). For the WILN system implementation, we have used the Generic Robot Navigation (GeRoNa)<sup>3</sup> library proposed by Huskić et al. (2019) to allow fast computation of the command vector  $\mathbf{u}$ .

At each time step, a control law is built to allow the robot to adjust its orientation to converge to the reference path  $\mathbf{x}_{ref}$ , as shown in [Figure 5](#). A Frenet-Serret frame  $\mathcal{S}$  is defined in the map frame. Its origin lies in the orthogonal projection of the robot frame  $\mathcal{R}$  on the reference path. After, an exponential function is defined to allow the robot to converge to the reference path, drawn in blue in [Figure 5](#). The angle of this exponential function is defined by

$$\phi_c = \arctan(-kx_n \exp(-kx_t)). \quad (3)$$

where  $k \in \mathbb{R}_{>0}$  is a constant that allows the regulation of the convergence speed of the robot to the path. We also denote  $x_t \in \mathbb{R}$  and  $x_n \in \mathbb{R}$  as the current position of  $\mathcal{R}$  in path frame  $\mathcal{S}$ , along the tangential  $\vec{x}_t$  and normal  $\vec{x}_n$  axis, respectively. Linear velocity is computed by modulating the target vehicle velocity  $v_n$ . Thus, the complete control law can be defined by

$$\mathbf{u} = \begin{bmatrix} v_x \\ \omega \end{bmatrix} = \begin{bmatrix} v_n \exp\left(-\left(\frac{K_g}{d_g}\right)\right) \\ K_h(\phi_c + \theta_e) \end{bmatrix} \quad (4)$$

where  $\theta_e \in \mathbb{R}_{>0}$  is the error between the robot angle  $\theta_r$  and the path frame angle  $\theta_t$  in the global frame  $\mathcal{G}$ . The  $K_h \in \mathbb{R}_{>0}$  parameter is a gain on commanded angular velocity that was added in order to reduce controller overshoot when subject to high reference path curvature  $\kappa$ . The distance between the current robot pose and the end of the trajectory is represented by  $d_g \in \mathbb{R}_{>0}$  and a goal proximity gain  $K_g \in \mathbb{R}_{>0}$  is defined to gradually slow the robot as it reaches its goal. To respect the limitations of the robotic platform, the commanded angular velocity is limited to  $\omega \in [-\omega_m, \omega_m]$ . The commanded linear velocity is bounded to  $v_x \in [v_{min}, v_{max}]$ . A goal tolerance  $\tau_g \in \mathbb{R}_{>0}$  parameter is used to allow the robot to finish the path repetition when within an acceptable distance from the  $\mathbf{x}_{ref}$  end. Finally, a safety tolerance  $\tau_w \in \mathbb{R}_{>0}$  parameter is defined to stop the robot if the distance between the origin of the robot's frame  $\mathcal{R}$  and the closest trajectory point of  $\mathbf{x}_{ref}$  exceeds the specified distance  $\tau_w$ .

An overview of the entire WILN pipeline is shown in [Figure 6](#). During the teach phase, an operator drives the robot along the desired trajectory. Sensor measurements are used to solve the SLAM problem and build a database

<sup>3</sup><https://github.com/cogsys-tuebingen/gerona>



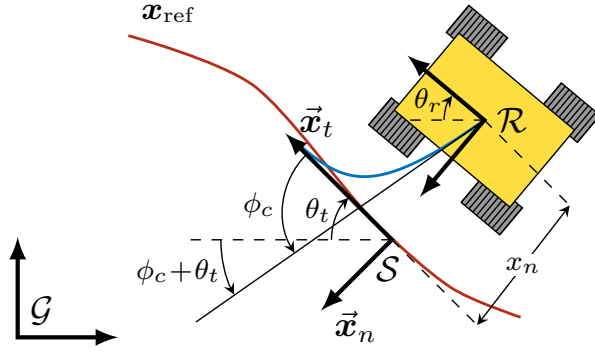


Figure 5: Main components of the Orthogonal-Exponential (OE) path-following algorithm used in this work. In red is the reference trajectory. In blue is the predicted exponential trajectory. The Frenet-Serret frame  $S$  is located on the referential trajectory.

containing all reference maps and trajectories. A point-cloud de-skewing system is used to take intra-scan lidar motion into account. This same system is used to produce a transformation prior  ${}^G_{\mathcal{L}}\tilde{T}$  to allow the ICP algorithm to perform real-time point cloud registration. A map maintenance module is used to append the latest registered lidar scan  ${}^G\mathcal{P}$  to the local map  ${}^G\mathcal{Q}$ . This module is also used to compute surface normals and remove dynamic points from the map, yielding the maintained map  ${}^G\mathcal{Q}'$ . Then, the *voxel manager* module is used to split the map into the latest local map  ${}^G\mathcal{Q}$  and non-local map  ${}^G\mathcal{Q}_{DB}$ . At the end of the teach phase, the entire map and reference trajectory  $x_{ref}$  are saved in the database for later use in the repeat phase. For the repeat phase, the ICP algorithm registers incoming lidar scans identically as in the teach phase. However, only the estimated robot pose  ${}^G_{\mathcal{L}}\hat{T}$  is used. The reference trajectory  $x_{ref}$  and current robot pose  ${}^G_{\mathcal{L}}\hat{T}$  are then sent to the path follower, which outputs the command vector  $u$ . Since no point clouds are appended to the map, no map maintenance module is used during the repeat phase. The *voxel manager* module is used to build the local and non-local maps; only the former is taken into account by the ICP algorithm.

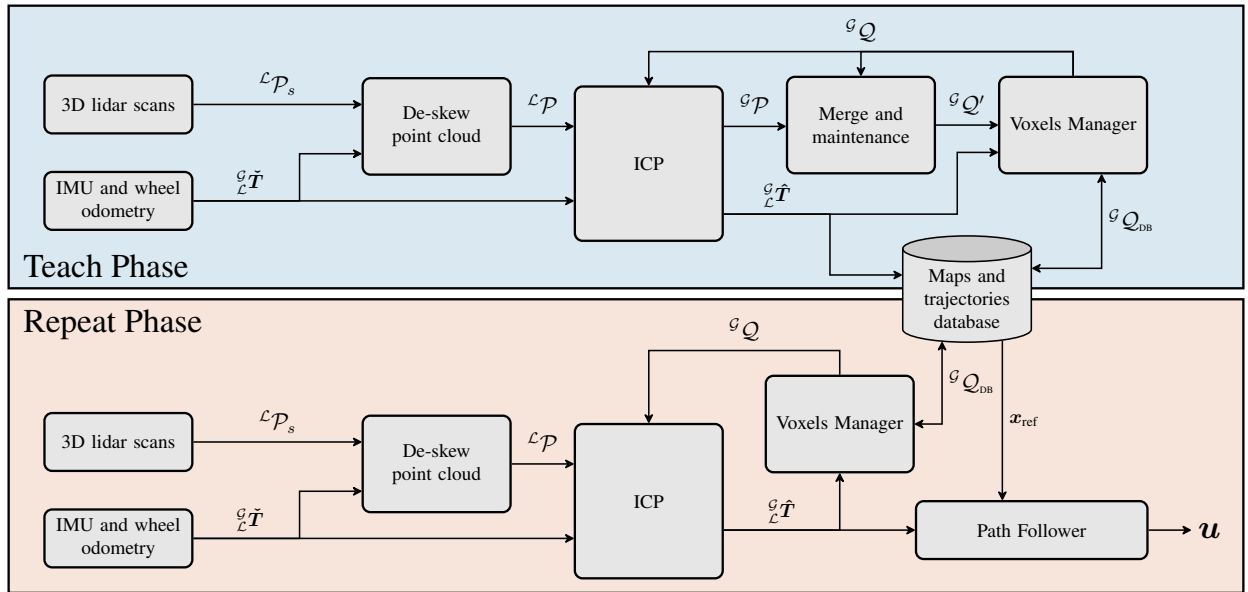


Figure 6: Overview of the WILN pipeline. The teach phase (in blue) takes as input the point clouds from the lidar and the odometry. The information is then used by the de-skewing algorithm and sent into ICP, which is used to solve the SLAM problem. At the end of the teach phase, the local  ${}^G\mathcal{Q}$  and non-local  ${}^G\mathcal{Q}_{DB}$  maps are saved in the database. The inputs of the repeat phase (in red) are the same as for the teach phase. The transformation outputted by ICP is finally used by the path follower to compute the commands sent to the vehicle.

## 4 Experimental setup

In this work, we conducted our deployment within the Montmorency boreal forest, located at a latitude of  $47^{\circ}19'15''\text{N}$  and a longitude of  $70^{\circ}9'0''\text{W}$ . The deployment took place during winter, creating ideal conditions to evaluate the impact snowfall and dense vegetation can have on autonomous navigation. The hardware used to perform autonomous navigation is weatherproof and can navigate steep and soft terrain. This section first describes the winter-resilient hardware used to deploy the WILN system, including the UGV, sensing and computing hardware. Next, details about the various implementation parameters presented throughout [Section 3](#) are given. Lastly, we list the characteristics of the Montmorency boreal forest, the weather and conditions to which our system was subjected when navigating.

### 4.1 Hardware description

Our system was deployed on a modified *Clearpath Robotics* Warthog UGV, as shown in [Figure 7](#). The Warthog is a Skid-steering mobile robot (SSMR) using two drive units located on each side of its chassis. For SSMRs, steering is done by rotating the wheels on each side of the vehicle at different velocities to create a skidding effect, effectively turning the vehicle. Vehicle motion control is achieved through a sub-servo system allowing each side’s wheel velocity to controlled through Sevcon Gen4 drives and wheel encoders signal. A kinematic linear mapping between wheel velocities and body velocities allows body-velocity commands to be sent directly to the platform. Instead of wheels, the Warthog is mounted on four CAMSO ATV T4S tracks to maximize mobility, as depicted in [Figure 7](#). The Warthog is also equipped with a differential suspension, maximizing traction when navigating steep terrain. A Robosense RS-32 3D lidar is mounted in front of the robot, with no pitch or roll inclination. This lidar has a 200 m detection range and produces about 640 000 points per second. Three Hall effect sensors are added to each motor to provide wheel odometry for the robot. Completing the WILN sensor package, an XSens MTi-10 IMU provides angular velocity and body linear acceleration measurements. Additionally, two Emlid Reach-RS+ RTK GNSS receivers were added to the robot chassis and a third was used as a fixed antenna to produce GNSS localization measurements. An Acrosser AIV-Q170V1FL on-board computer is used to record sensor data and perform all of the WILN system computation. All technical specifications for the platform are given in [Figure 7](#).

	Characteristics	Value
Physical	Mass	590 kg
	Footprint	$2.13 \text{ m} \times 1.52 \text{ m}$
	Top speed	18 km/h
	Steering geometry	Skid-steering
	Locomotion	CAMSO ATV T4S Tracks
	Suspension	Geometric Passive Articulation
Sensors	Lidar	Robosense RS-32 (10 Hz)
	IMU	XSens MTi-10 (100 Hz)
	Wheel encoders	3 x Hall effect sensors (4 Hz)
	GNSS	Emlid Reach-RS+ (5 Hz)
Computing	Computer	Acrosser AIV-Q170V1FL
	CPU	i7-6700 TE (3.40 GHz)
	↳ Number of cores	4
	↳ Number of threads	8
	↳ RAM	16 Gb



Figure 7: Experimental setup for the WILN system on our Clearpath Robotics Warthog UGV. Left : Detailed specifications. Right: The numbers in red circles correspond to (1) Robosense RS-32 lidar, (2) XSens MTi-10 IMU, (3) two Emlid Reach-RS+ GNSS antennas. The two GNSS antennas are not used for the localization of the WILN system.

## 4.2 Implementation parameters

To allow the WILN framework to perform large-scale navigation, we hand-tuned the parameters of each subsystem. All parameters are enumerated in [Section 3](#). Without conducting extensive calibration, we let the system repeat several short paths and manually adjusted parameters until observing stable performance. For this work, parameters were tuned to reach a working state for the WILN system, but no sensitivity analysis was conducted. Our goal was to evaluate the impact of the boreal forest and winter conditions on the system without extensive effort on system calibration. The mapping subsystem had three distinct goals: enabling point cloud registration by computing surface normals, maintaining the map to remove dynamic points and splitting the map into local and non-local through the *voxel manager*. This would prevent localization failures during repeat runs. Path-following overshoot in tight curves and controller oscillations were also minimized by adjusting the parameters. An overview of the tuned parameters is provided in [Table 1](#).

Table 1: Parameter values related to each function used in our system. Functions and parameters are split between the registration, mapping and control subsystems. All functions and parameters are detailed in [Section 3](#).

	Function	Parameters
ICP	Bounding box input filter 1	$\mathbf{b}_1 = [-1.5 \text{ m}, 0.5 \text{ m}, -1 \text{ m}, 1 \text{ m}, -1 \text{ m}, 0.5 \text{ m}]$
	Bounding box input filter 2	$\mathbf{b}_2 = [-10 \text{ m}, -1.5 \text{ m}, -2.5 \text{ m}, 2.5 \text{ m}, -1 \text{ m}, 1 \text{ m}]$
	Random sampling input filter	$\eta_s = 0.7$
	Maximum radius input filter	$r = 80 \text{ m}$
	KD tree matcher	$n_m = 7 \quad \varepsilon = 1 \quad d_{\max} = 2.0 \text{ m}$
	Trimmed distance outlier filter	$\eta_d = 0.7$
	Differential transformation checker	$\varepsilon_{\theta_{\min}} = 0.001 \quad \varepsilon_{t_{\min}} = 0.01$
	Counter transformation checker	$i_{\max} = 40$
Mapping	Large scale mapping	$\rho = 0.1 \text{ m} \quad v_s = 20 \text{ m}$
	Surface normal points filter	$n_n = 15$
	Dynamic points filter	$\tau_d = 0.8$
Path-following	Waypoint tolerance	$\tau_w = 1.0 \text{ m}$
	Goal tolerance	$\tau_g = 0.15 \text{ m}$
	Regulator path convergence	$k = 0.4$
	Compensation angular speed command	$K_h = 3.0$
	Max angular velocity	$\omega_m = 1.0 \text{ rad s}^{-1}$
	Goal position factor	$K_g = 0.5$
	Linear nominal speed	$v_{\text{nom}} = 1.5 \text{ m s}^{-1}$
	Linear minimal speed	$v_{\min} = 0.5 \text{ m s}^{-1}$
	Linear maximal speed	$v_{\max} = 1.5 \text{ m s}^{-1}$
	Reference trajectory pose distance	$d_{\text{ref}} = 5 \text{ cm}$

## 4.3 Environment

For this work, autonomous navigation was conducted in the Montmorency boreal forest. This environment is ideal to help highlight how dense vegetation and snow precipitation affects the performance of lidar and GNSS-based autonomous navigation, which are the main contributions of this paper. A digital terrain model of the deployment area, with a representation of the path network is shown in [Figure 8](#). It can be seen that three different paths were defined, all linking two Points of Interests (POIs). The goal of defining three different paths is to highlight the difference in localization performance between the two path types. Path A links the Garage and Cabin POIs through a cross-country ski trail and has the total distance of 1.4 km. According to guidelines, we expect this ski trail to have a minimal width of 4.5 m (*Ministère des Forêts, de la Faune et des Parcs*, 2017). Path B also links the Garage and Cabin POIs and has a total distance of 1.5 km. Path B is identical to path A for the first third of the path and then diverts to a foot

trail, where the width is similar to the one observed on path A. We observed that multiple areas of path B have a lower width than the expected 4.5 m since this is a foot trail. To prevent UGV immobilization, the snow on paths A and B had been compacted by a snowmobile operator prior to the experiment. Path C connects the Garage and Gazebo POIs mostly through a network of wider roads and has a total distance of 0.5 km. Path C corresponds to a forest road, with a minimum width of 9.1 m according to official guidelines of the Montmorency boreal forest (*Ministère des Forêts, de la Faune et des Parcs*, 2021). It should be noted that path C was conducted as a round-trip path, consisting of a forward pass and a backward pass. This choice was made to increase autonomous navigation data and include data with the UGV driving in both directions. Also, it can be observed in the Above Mean Sea Level (AMSL) model in Figure 8 that the path network is located in a valley, surrounded by various mountains.

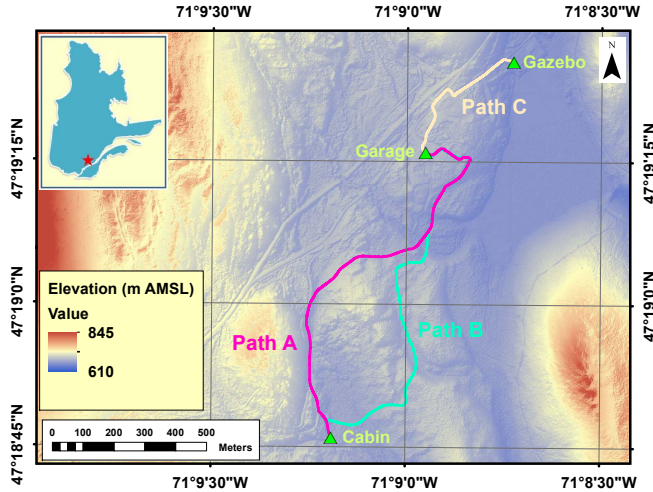


Figure 8: A digital terrain model of the Montmorency forest, where the WILN system was deployed and the forest location in Québec, Canada (top left). We see the three different paths, both paths A (1.4 km) and B (1.5 km) going from the garage POI to the Cabin POI, while path C (0.5 km) connects the Garage POI to the Gazebo POI. Global latitudinal and longitudinal coordinates are given in the margin. The coloring is defined by AMSL elevation. Image credit : Remote and Wood Sensing Laboratory, University of New Brunswick.

During the deployment week, the WILN system was subjected to fluctuating weather, including light and heavy snow, hail and drizzle. We have access to extensive data gathered through a meteorological station located at the Montmorency forest. The area temperature was measured with a temperature probe of model 107 made by *Campbell Sci.*, which was covered by an anti radiation screen two meters away from the ground. The precipitation type was measured with a Parsivel<sup>2</sup> disdrometer made by *OTT*. An overview of the meteorological conditions is illustrated in Figure 9. Outside temperatures ranged from  $-15.5^{\circ}\text{C}$  to  $13.4^{\circ}\text{C}$ . The temperature fluctuating over and under the water freezing point (i.e.,  $0^{\circ}\text{C}$ ), meaning that snow in the environment melted on some occasions and froze on others, effectively accumulating on the ground. Teach runs (i.e., TA, TB and TC) were conducted when there was no precipitation. Runs R1 through R7 were conducted in rainy weather, while runs R8 through R12 were conducted in snowfall. The standard for weather codes shown in Figure 9 is code table 4680 for automatic weather stations (World Meteorological Organization, 2019). During runs R13 and R14, the system was not subject to any precipitation. While not shown in this figure, we performed autonomous repeats during both daytime and nighttime, with no impact on system performance. More details on each run are given in Section 5.

## 5 Results

The two main goals of this work are to evaluate the impact of the boreal forest and winter weather on autonomous navigation performance. First, we document all three distinct reference maps and trajectories that were built through the teach phase. Then, we report on all repeat runs that were conducted over the deployment week. As a prior to further analysis, general information on all runs conducted during the deployment are presented. Afterwards, we highlight the effects of the boreal forest, more specifically of the dense vegetation, on GNSS-based and ICP-based localization in Section 5.1. Then, Section 5.2 describes how snow accumulation induces significant change in the environment landscape, resulting in ICP localization failures. Finally, Section 5.3 explains the impact of the environment on the OE controller path-following performance.

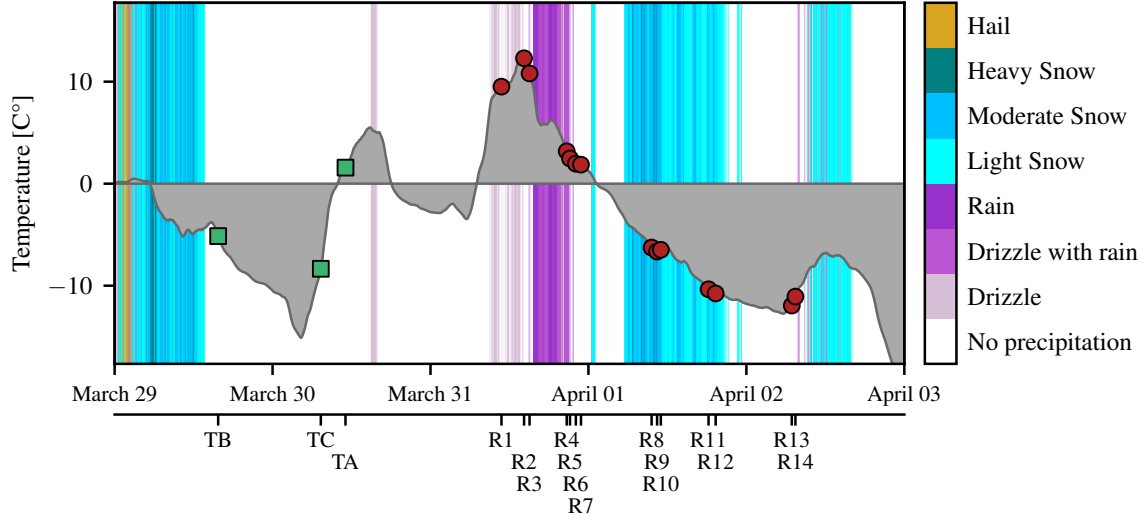


Figure 9: Temperature and weather during the deployment. Teach runs are depicted in green squares whereas Repeat runs are depicted in red circles. Teach runs have been performed in relatively clear weather, while repeat runs suffered from rain and different levels of snowfall.

Teach runs were performed to record the reference maps  $^G Q_{DB}$  and the trajectories  $x_{ref}$  for all three paths. During these runs, we manually drove the robot, while the map and trajectory database were built online. The resulting maps for each path are illustrated in Figure 10 with the coordinates defined in the map frame  $\mathcal{G}$  specific to each path. In this visualization, the  $z$  component of the estimated surface normal vector is used to color each point. Thus, dark blue points represent walls, as can be seen on the  $C$  path, green points typically represent vegetation and yellow points represent ground surfaces. Paths  $A$  and  $B$  are mostly located within dense vegetation. On the other hand, the path  $C$  is located on a much more open forest road. Table 2 presents relevant details about each of the teach and repeat runs conducted during the deployment. A total of 14 repeat runs were completed, summing up to 18.6 km and 7 h 13 min of autonomous repeating over five days. The last repeat run was started over 87 h after its respective teach run on path  $B$ . A battery breakdown prevented us from completing run **R7**; it was therefore interrupted. For each run, the sun radiation measured by a  $CNR4$  radiometer equipped with a  $CNF4$  ventilation unit made by Kipp & Zonen located within the forest is given.

## 5.1 Impact of the boreal forest biome

The first main goal of this work is to evaluate the impact of dense vegetation inherent to boreal forests on both GNSS and lidar-based localization for autonomous navigation. During all repeat runs, the GNSS signal statistics were logged in both receivers mounted on the Warthog UGV. Additionally, measurements were taken from a fixed reference receiver during each run to enable RTK-GNSS positioning. The data were post-processed offline using RTKLIB<sup>4</sup> (Takasu & Yasuda, 2009) to produce the most accurate measurements possible. To estimate the GNSS localization error, we compared the manually measured distance between the GNSS receivers mounted on the UGV with the distance indicated by the GNSS localization, similarly as in (Vaidis et al., 2021). This metric does not take into account localization biases to which both receivers might be subjected, thus we consider the error metric an optimistic one. The results of the GNSS error with respect to the mean number of satellites between the two mobile receivers are presented in Figure 11. Our dataset does not contain a sufficient number of data points with less than seven satellites, we therefore exclude them from our analysis. This shows that for reliable GNSS localization on forest trails, the minimum number of observed satellites  $n_{cs}$  is 18. If a lower number of satellites is observed, the system is at risk of collision with the vegetation at the edges of the path. Since the off-road paths are wider, they allow slightly lower  $n_{cs}$  of 16.5 for safe navigation.

<sup>4</sup><http://www.rtklib.com/>



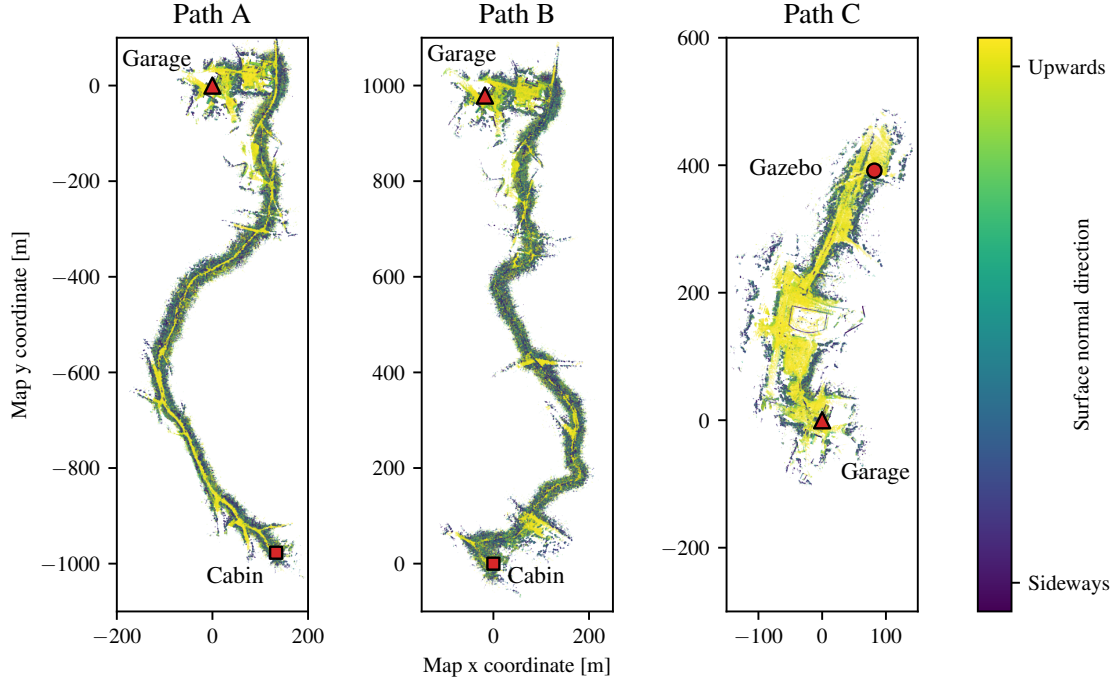


Figure 10: All reference maps recorded during the three teach phases for this work. The colormap represents the  $z$  component of the surface normal for all points in the map. Yellow points are the ones with the surface normal pointing upwards. Green and dark blue points have a surface normal pointing sideways. The red markers represent the reference trajectory POIs. All maps have been rotated in order to allow visualization in the same figure.

Table 2: Overview of all runs conducted in this work. All times are defined in the local Eastern Standard Time.  $A'$  or  $B'$  means the run started at the Cabin POI. The column  $\Delta t$  defines the elapsed time since the teach run of the associated path. The column  $\# \mathcal{P}$  shows the number of scans for each run. The illumination measured at the start of each run is given. Teach runs are not accounted for in the total autonomous distance recorded.

ID	Path	Start time (2021)	Duration (hh:mm)	$\Delta t$ (hh:mm)	$\# \mathcal{P}$	Distance (km)	Illumination ( $\text{W m}^{-2}$ )
TB	$B'$	March 29th 15:46	00:27	00:00	15 715	1.5	283.35
R2	$B$	March 31st 14:12	00:27	46:26	16 183	1.5	295.10
R5	$B'$	March 31st 21:14	00:27	53:28	16 056	1.5	0.00
R6	$B$	March 31st 22:05	00:27	54:19	16 163	1.5	0.00
R9	$B'$	April 1st 10:27	00:27	66:41	16 093	1.5	123.90
R11	$B$	April 1st 18:18	00:32	74:32	19 443	1.5	0.75
R14	$B'$	April 2nd 07:28	00:27	87:42	16 073	1.5	188.42
TC	$C$	March 30th 07:29	00:21	00:00	12 762	1.0	102.58
R1	$C$	March 31st 10:46	00:23	27:17	13 758	1.0	284.80
R10	$C$	April 1st 11:03	00:20	51:34	12 162	1.0	159.23
TA	$A$	March 30th 11:06	00:25	00:00	15 142	1.4	586.38
R3	$A'$	March 31st 15:04	00:26	27:58	15 535	1.4	101.55
R4	$A$	March 31st 20:44	00:26	33:38	15 641	1.4	0.00
<b>R7</b>	$A'$	March 31st 22:49	00:15	35:43	8862	<b>0.6</b>	0.00
R8	$A$	April 1st 09:25	00:28	46:19	15 623	1.4	84.68
R12	$A'$	April 1st 19:19	00:29	56:13	17 218	1.4	0.00
R13	$A$	April 2nd 06:55	00:26	67:49	15 583	1.4	99.63
Total	17 runs	–	07:13	–	258 012	18.6	–

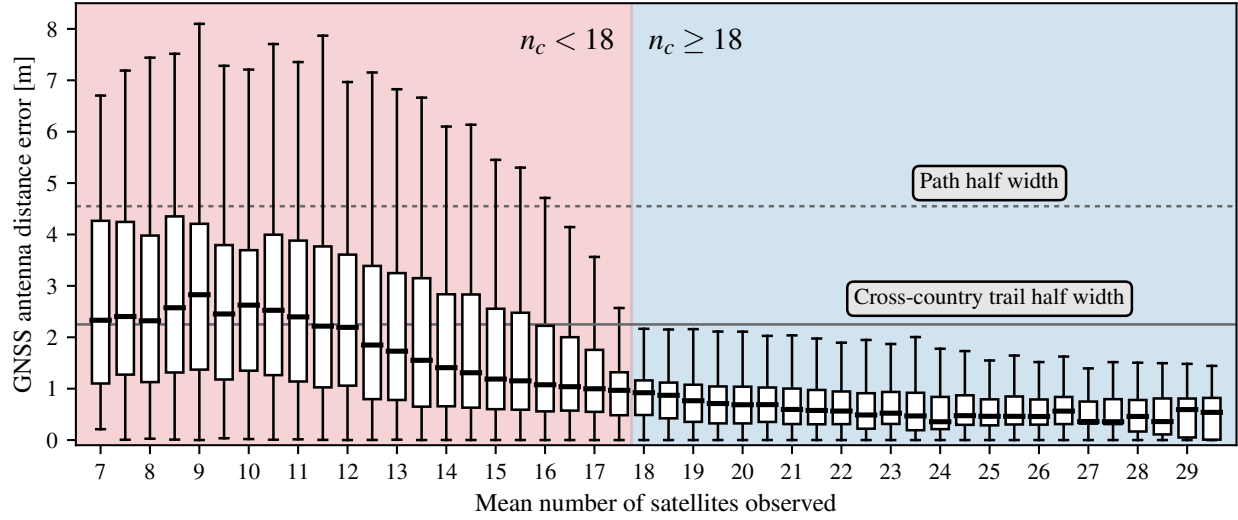


Figure 11: GNSS error with respect to the mean number of observed satellites between the two receivers mounted on the UGV over all runs. The thick black lines represent medians, the boxes represent the first and third quartiles, and the whiskers represent the 10<sup>th</sup> and 90<sup>th</sup> percentiles. The expected forest road and forest trail half-widths are 4.55 m and 2.25 m respectively. The shaded blue area denotes the acceptable number of observed satellites for reliable navigation in wood trails. The area in red is unacceptable for forest trail navigation, based on the critical threshold  $n_c$ .

Based on the critical number of satellites determined in [Figure 11](#), we have conducted an analysis of all reference trajectories to determine the areas considered to be GNSS-denied. [Figure 12](#) shows the mean number of observed satellites in a geo-referenced satellite image. On the paths A and B, the mean number of satellites drops below the critical number  $n_c$  at several locations, mostly in areas located within dense vegetation. The mean number of observed satellites increases over  $n_c$  in the open areas of the trail network. Path C is the only path that could be repeated reliably using GNSS localization. This is due to the fact that its environment is considerably more open compared to A and B, as shown in [Figure 10](#). Additionally, it is necessary to stress that to achieve the presented accuracy in real time, a stable data link between the mobile GNSS receivers and the reference receiver must be maintained. In practice, this data link is usually implemented by a radio link or by a mobile internet connection, which can be complex to set up in remote locations. In our case, the reference receiver radio signal could not cover the entirety of the A and B paths. Yet, we confirm that the reference receiver positioned on an elevated spot which is not occluded by trees (i.e., A1) provides better range compared to the locations A2 and A3 in the forest.

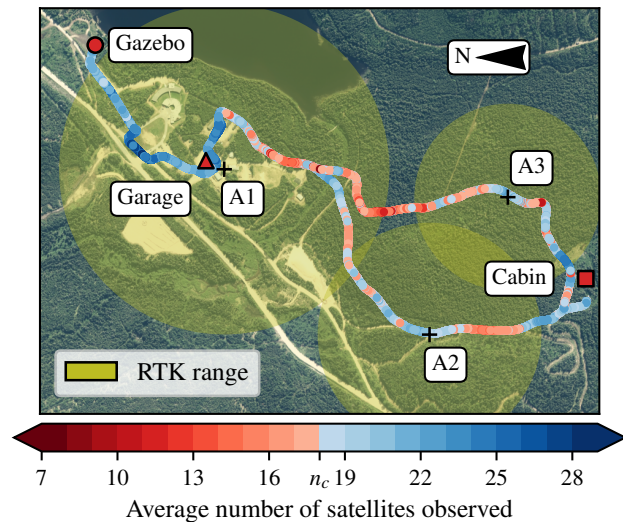


Figure 12: GNSS satellites coverage along the reference trajectories. The blue palette is used for the sections where the GNSS accuracy would be sufficient for the width of the trail. The red sections would not allow pure GNSS navigation. For RTK-GNSS localization, the distinct positions of the reference receiver are the A1, A2 and A3 points. The radio signal range of the reference receivers is shown in olive. Image credit: Forêt ouverte.

Furthermore, the ICP algorithm provided localization accurate enough to allow the robot to complete each repeat run without colliding with obstacles. Yet, we observed that the corridor-like nature of the boreal forest trails leads to a high localization uncertainty. To investigate this phenomenon, we extracted 500 lidar scans  $\mathcal{P}$  from runs R4, R5 and R1, uniformly distributed time-wise, all of which are shown in Figure 13. These runs are the first repeat runs conducted in the same direction for each reference path. For each lidar scan  $\mathcal{P}$ , we expressed the map  $\mathcal{Q}$  in the corresponding lidar frame  $\mathcal{L}$ . The initially well-registered scans were perturbed along the robot's longitudinal axis by translations from  $-6$  m to  $6$  m with increments of  $0.05$  m. The point-to-plane error  $e$ , defined in Equation 2 was then evaluated for each perturbed scan with respect to the reference  $\mathcal{Q}$ . The standard deviation of the error was used to color each scan.

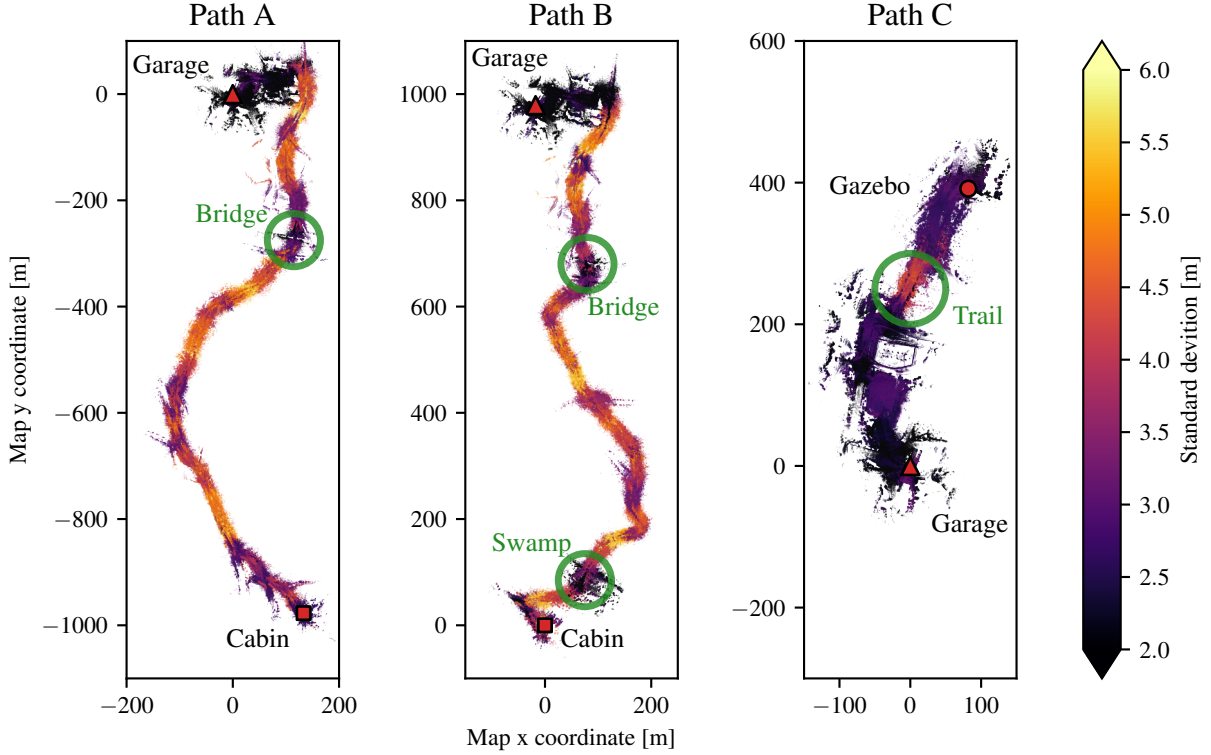


Figure 13: Top view of a set of 500 lidar scans  $\mathcal{G}\mathcal{P}$  from runs R4, R5 and R1, conducted on paths A, B and C, respectively. All of the scans are distributed evenly time-wise in their respective runs. The standard deviation of the point-to-plane error  $e$  after applying perturbations is used to color each scan. A higher standard deviation is linked to a higher localization uncertainty. Distinctive areas are highlighted by the green circles. The starting and ending POIs for each trajectory are denoted by the red markers.

The areas located within the cross-country skiing trails are related to a considerably higher standard deviation. Indeed, the ICP error function, presented in Equation 2, is much flatter in such areas. A pattern emerges: the standard deviation increases when the robot traverses long and narrow forest corridors, and then decreases when driving through trail intersections. Moreover, the standard deviation in the *Bridge* area, located in paths A and B, decreases notably compared to its surroundings. The river breaks the line of trees in this area and provides additional geometrical constraints, effectively improving the localization accuracy. A similar effect can be observed in the *Swamp* area in path B. A considerable amount of vegetation is perpendicular to the longitudinal direction of the robot, better constraining the registration error function. Analogously, the results from path C demonstrate that the standard deviation is much lower in the wide forest paths. The only place where the localization uncertainty increases again is the narrow trail area marked by the green circle.

## 5.2 Impact of snow precipitation and accumulation

Another important goal of the deployment was to study the impact of winter weather on autonomous navigation. Paton et al. (2017) already mentioned illumination variation, low feature contrast and a changing environment as issues for vision-based navigation. Thus, in this work, we focus on the impact of snow precipitation on lidar-based localization. While the system was deployed under various weather conditions, as shown in Figure 9, we did not observe any correlation between the precipitation and the immediate accuracy of localization. However, the snow accumulation led to significant changes in the environment, which affected the ability of our system to localize between teach and repeat runs. More specifically, the WILN system failed to initialize its localization in the reference map during two attempts to start run R9. The third attempt was successful, and the system repeated the entire path without fail subsequently. As documented by Figure 9, run R9 was conducted right after moderate snowfall, and there was thus a significant amount of snow accumulation in the environment.

To analyze the impact of snow accumulation on the reliability of the lidar-based localization, we extracted 500 lidar scans  $\mathcal{GP}$  from runs R5, R9 and R14. These scans were already registered with the map and are distributed evenly with respect to time. All three runs were conducted on path  $B$  from the Cabin POI to the Garage POI. Then, we evaluated the overlap percentage for each  $\mathcal{GP}$  scan, presented in Figure 14. A scan point was considered as overlapping the map if it was located closer than 0.5 m to any  $\mathcal{Q}$  point.

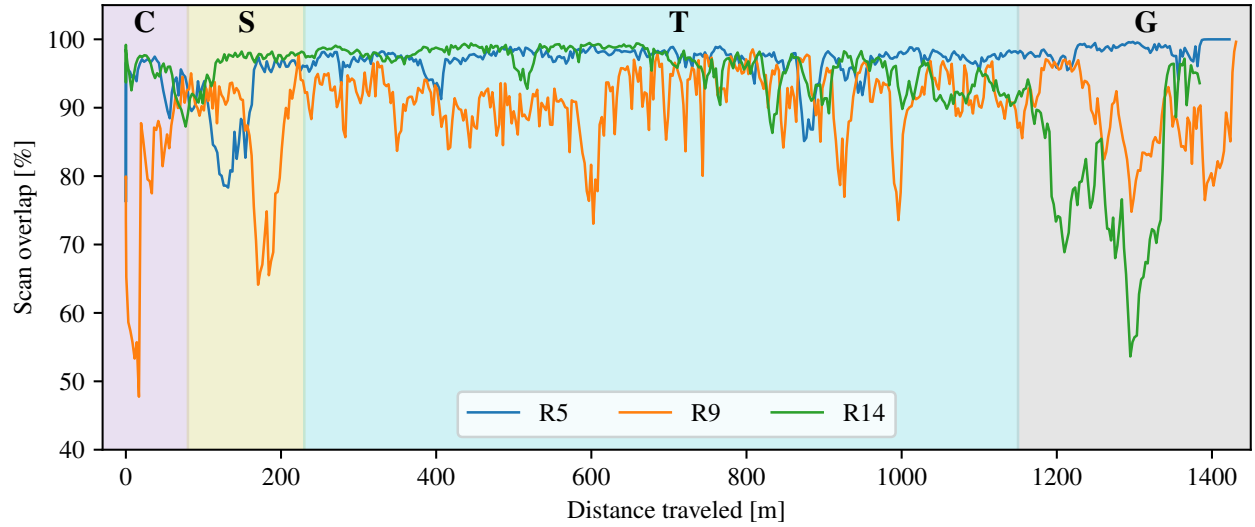


Figure 14: Overlapping percentage of lidar scans  $\mathcal{GP}$  on the reference map  $\mathcal{GQ}$ . The results from runs R5, R9 and R14 are plotted in blue, orange and green, respectively. The shaded **C** area represents the *Cabin* area, **S** represents the *Swamp* area, **T** represents the *Trails* area and **G** represents the *Garage* area.

It is apparent that the scan overlap in run R9 is considerably lower than the scan overlap in R5 and R14, except for the garage area, where R14 has the lowest scan overlap. For the *Cabin*, *Swamp* and *Trails* areas, the lower overlap ratio can be attributed to snow that accumulated in the environment, which was significantly higher in R9 due to snowfall. Specifically for the *Cabin* area, the large drop in the scan overlap explains the multiple failed initialization attempts mentioned earlier. Furthermore, looking at the *Garage* area, it can be seen that scan overlap decreases as time progresses. Indeed, intermittent snow plowing operations were conducted in this area. Growing snowbanks at the edge of the road, led to dynamic changes in the area landscape and consequently to a progressive decrease in lidar scan overlap with the reference map, as shown in Figure 14. As specific examples, we extracted four problematic areas related to snow accumulation, all of which are shown in Figure 15. A red color mask was applied to the lidar scans  $\mathcal{P}$  in Figure 15 to highlight the non-overlapping points.

In the *Cabin* area during run R9, it is apparent that snow accumulation led to a variation in the terrain steepness, which affected the ability of the ICP algorithm to initialize its localization within the reference map. The difference in the scan overlap between run R9 and other runs is also noticeable in the *Swamp* and *Trail* areas, although to a lesser



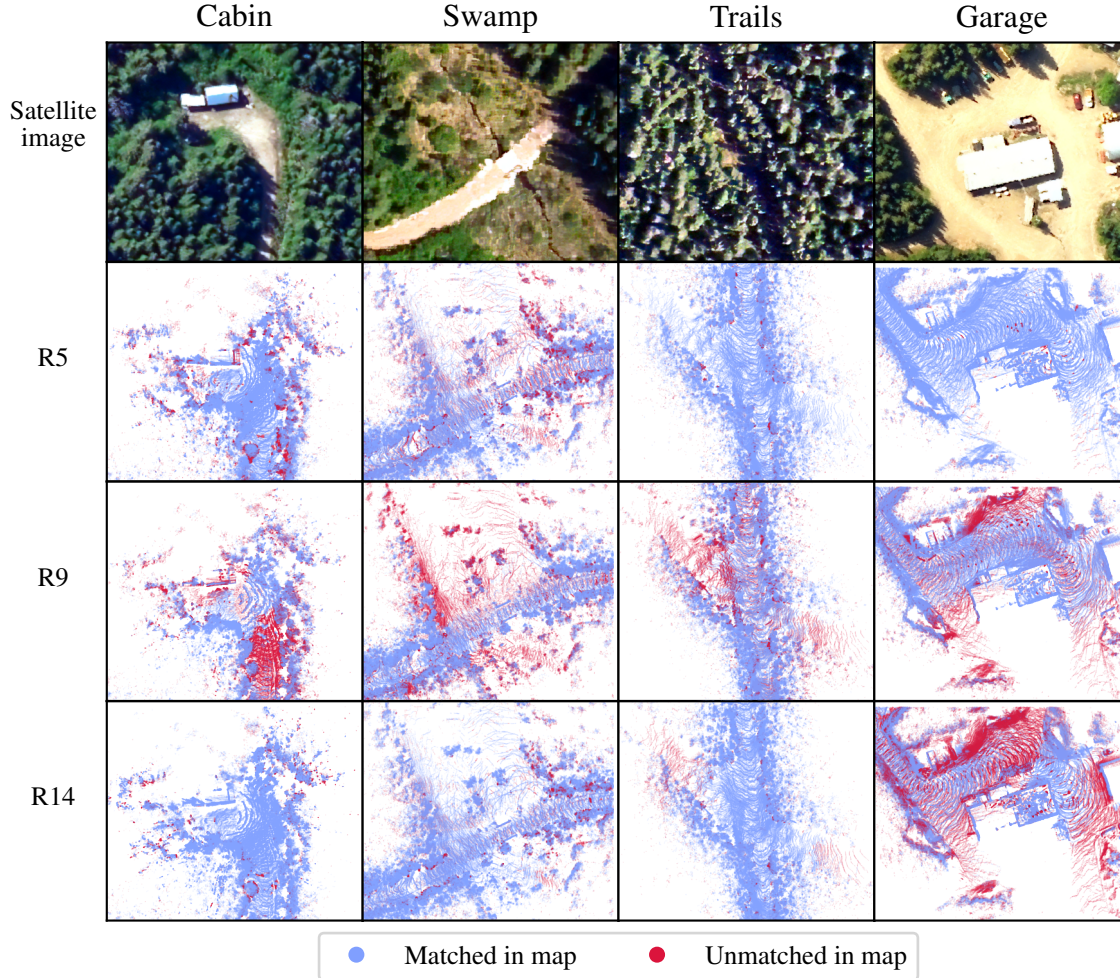


Figure 15: A detail of various parts of the B path. The satellite images in the top row illustrate the locations. In the registered lidar scans from runs R5, R9 and R14, the points are colored blue if they have a counterpart in the reference map. Contrarily, red points miss their map counterpart and mark a new feature or a change in the environment.

extent. Following what is shown in [Figure 14](#), the overlap percentage in the *Garage* area was gradually decreasing as time passed. This phenomenon was related to the aforementioned snow plowing operation taking place in that area, effectively changing the snow landscape. During the run R14, there was also a large truck parked near the *Garage*, which contributed to the unmatched points. It should be noted that while scan overlap reaches low values in the *Garage* area, the WILN system did not suffer from localization failure during any run in this area. The location contains multiple buildings, resulting in a higher number of geometrical constraints, allowing the ICP algorithm to localize the robot despite variations in landscape. We assume that the scan overlap would continue to decrease as more time is elapsed between a repeat run and its respective teach run.

### 5.3 Motion and control

To characterize the performance of our path-following controller, we computed the cross-track error, which is the distance between the robot frame  $\mathcal{R}$ 's origin and its orthogonal projection on the path, as defined by Mondoloni et al. (2005). The median cross-track error across all *A*, *B* and *C* paths runs is 0.083 m, 0.088 m and 0.075 m respectively. The maximum observed cross-track errors across all runs is 1.19 m for path *A*, 1.17 m for path *B* and 0.92 m for path



C. These results suggest that the path-following performance slightly decreases when navigating on a forest trail (i.e., paths *A* and *B*), compared to the forest road (i.e., path *C*). When comparing the results, we did not observe a correlation between weather conditions and cross-track error.

Nonetheless, we did observe significant correlation between path curvature and cross-track error. To analyze this phenomenon, we estimated the path curvature  $\kappa$  of each reference trajectory points. To remove localization noise from the curvature computation, we took ten nearest reference trajectory points into account. We then sub-sampled all repeat trajectories to keep points at a distance of 0.1 m from each other. For each point of the sub-sampled trajectories, we found the closest reference trajectory point, computed the cross track error  $\epsilon_{CT}$  and associated it with the reference point's curvature  $\kappa$ . This computation allows us to correlate path curvature with cross track error, as shown in Figure 16.

We detect that cross-track error increases proportionally to the path curvature. For low curves (i.e., the first six bins), the 90<sup>th</sup> percentile of the cross-track errors remains below 0.6 m. For straight lines (i.e., the first bin), we attribute the excessive errors over 0.6 m to the initialization error in the beginning of the repeat runs. When navigating in moderate turns (i.e., the last two bins), the 90<sup>th</sup> percentile of cross-track errors reaches 1.0 m. Due to limitations of the OE controller, the system did not navigate in tight curves (i.e., turning on the spot). The high motion prediction inaccuracy of the kinematic differential-drive model when turning at high angular velocities is the cause for this high increase in cross-track error, as highlighted by Baril et al. (2020). While this error is below the cross-country trail half-width of 2.25 m, which we consider the limit for safe navigation in forest trails, it remains high. It should be noted that the repeat runs were conducted at a conservative nominal velocity  $v_{\text{nom}}$  of  $1.5 \text{ m s}^{-1}$ . Therefore, there is a significant risk of hitting vegetation for autonomous systems relying on kinematic controllers when navigating in a boreal forest at higher nominal velocities.

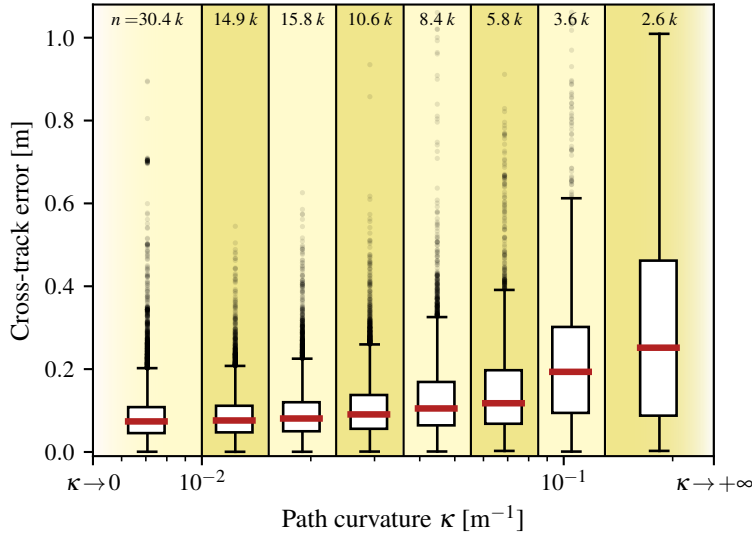


Figure 16: Cross-track error as a function of path curvature for all repeat runs. All errors were split into bins representing different path curvatures. The thick red lines represent medians, the boxes represent the first and third quartiles respectively and the whiskers represent the 10<sup>th</sup> and 90<sup>th</sup> percentiles. The path curvatures on abscissa are defined in a logarithmic scale. All data related to path curvatures smaller than  $0.01 \text{ m}^{-1}$  is grouped in the first bin. Similarly, all data related to path curvatures greater than or equal to  $0.13 \text{ m}^{-1}$  is grouped in the last bin.

## 6 Discussion

In this section, we use the results presented in Section 5 to elaborate how autonomous navigation algorithms should be improved to enable multi-year autonomy. We explain the challenges related to navigating tight forest trails with dense vegetation. We also argue that localization algorithms should adapt to dynamic environments to be deployed all-year long in northern environments. Moreover, we discuss the limitations of kinematic and time-invariant path-following controllers and the risk associated with robot immobilization when navigating in deep snow or through multiple seasons.

## 6.1 The forest corridor effect

We have highlighted the impact of the dense vegetation on GNSS signal reception in [Section 5.1](#). A typical example of a forest trail is shown in [Figure 1b](#). Because of the tree canopy, the GNSS signal is partially blocked or reflected, causing a drop in the number of visible satellites. This results in an excessively high error on GNSS localization when navigating within forest trails, as shown in [Figure 12](#). We observed that GNSS-based localization enables autonomous navigation on forest roads (i.e., path C), but the signal is not reliable when navigating boreal forest trails (i.e., paths A and B). Thus, completely autonomous navigation in a boreal forest requires a localization framework that is resilient to GNSS-denied conditions.

Moreover, we showed in [Section 5.1](#) that featureless corridors are challenging for lidar-based localization algorithms. As can be observed in [Figure 13](#), the uniform nature of boreal forest vegetation leads to low geometrical constraints in the robot's longitudinal direction. Low geometrical constraints lead to high registration uncertainty for the ICP algorithm, as highlighted by Gelfand et al. (2003). This lack of features makes the ICP registration cost function flat in the corresponding direction and sensitive to noise in the lidar measurements. We observe a similar phenomenon in the forest trails surrounded by dense vegetation. Since the lidar scans are not dense enough to distinguish between single branches, the trees resemble large blobs of randomly distributed points in the scans and ultimately in the map. Therefore, point cloud degradation is not limited to the large open areas that were mentioned by Ren et al. (2021). In particular, we have observed that point cloud degradation led to the ICP localization to jump forwards of up to 0.5 m. Such jumps in ICP localization lead to instability and eventually to system failure. Also, they disrupt the function of motion controllers, leading to jerky motion. A system aware of this phenomenon could potentially reduce its velocity in the problematic areas to prevent system failure. A more accurate and adaptive motion prediction model, similar to the one discussed in [Section 6.3](#) could also allow prior error to be reduced and improve localization resiliency in forest corridors.

## 6.2 Impact of snow accumulation

Our initial hypothesis was that during snowstorms, the precipitation would affect the localization accuracy of the ICP algorithm. Yet, as highlighted in [Section 5.2](#), we found no correlation between precipitation intensity and localization accuracy. Rather, we discovered that it was the snow accumulation that severely affected the lidar-based localization. On certain surface types, such as the ground or rooftops, the snow keeps accumulating during the snowstorms, as can be seen in [Figure 15](#). Yet on other surfaces (e.g., trees or running water), only a limited amount accumulates before it falls off or melts. Our data show that lidar-based localization in areas located within deep woods suffer from changes in terrain topology, while areas located near buildings are resilient to this phenomenon. A specific example of failure cases was observed when robot localization would fail on runs following snowfall. Localization failure resulted in the robot colliding with vegetation, as shown in [Figure 17](#). Nevertheless, autonomous systems should adapt their reference maps when observing a mismatch between the current sensor measurements and the reference data to ensure a complete, year-long autonomy.



Figure 17: The result of a failed localization initialization, during run R10. The high initial error in robot pose resulted in the Warthog diverging from the reference path and heading towards vegetation. The robot reached a 2.25 m deviation before being manually stopped and driven back to the initialization position.

### 6.3 Path following in snow-covered terrain

In [Section 5.3](#), we described the performance of the OE controller when used on the Warthog SSMR. We showed that when navigating at the target velocity  $v_{\text{nom}}$  of  $1.5 \text{ m s}^{-1}$ , this controller is able to repeat kilometer-scale paths, with an error that remains below the half-width of the forest trails. This result is interesting considering that the OE requires little knowledge of the UGV properties and has low computation time. We have observed that path curvature increases cross-track error, as depicted in [Figure 16](#). This suggests that SSMRs motion is difficult to predict when rotating at higher velocities. Thus, we can assume that navigation at higher nominal velocities would potentially lead to the robot crashing into the vegetation. Additionally, the OE controller does not react to UGV immobilization. This poses a high risk in off-road navigation, as [Figure 18c](#) and [Figure 20a](#) demonstrate. A controller based on a more accurate dynamic model that adapts to the various conditions would enable path repeating at higher speeds without failing. A model that can adapt to the differences in UGV behavior across the entire reference trajectory would also improve the path-following resiliency to WILN navigation in steep and soft terrain. We also argue that autonomous navigation algorithms should keep a memory of areas where the robot became immobilized in previous runs. Such areas should then be considered obstacles and avoided by local path planning algorithms, the same way they would avoid a fallen tree or a concrete block.

### 6.4 Effect of high speed navigation on localization

During our preliminary tests, we noticed that the WILN system was not robust to quick motions of the robot. When the robot rotated too quickly, the localization would fail because of motion distortions in lidar scans. To solve this issue, we added a point cloud de-skewing step, as described in [Section 3.1](#), to correct motion distortions. This solution was sufficient in our case because the robot was driven at the relatively low speed of  $1.5 \text{ m s}^{-1}$ . However, at higher speeds, motion distortion in lidar scans is more important and odometry accuracy is decreased because of slipping, skidding and potential robot immobilization. To solve this issue, we introduced an algorithm that computes the uncertainty of each point of a lidar scan to know which points can be trusted ([Deschênes et al., 2021](#)). Points which are likely to be more affected by motion distortion have a higher uncertainty than others, thus are given less influence during the registration process. Also, points which are too uncertain can be completely removed from the map to make sure that it stays crisp. This uncertainty-based algorithm, which can be used in combination with de-skewing algorithms, would help to preserve localization and mapping precision when navigating at high-speeds with the WILN system.

### 6.5 Lessons learned from field deployments

Through the multiple deployments conducted in the completion of this field report, we have learned various lessons that apply to generally to deploying mobile robots in northern environments. We have observed multiple issues related to robot navigation in deep snow, to localization uncertainty in forest corridor and to the winter weather affecting robot autonomy. We argue that autonomous systems need to be resilient to these challenges to enable true long-term autonomy. Additionally, we present various logistical difficulties that we encountered in the context of our deployments in the Montmorency forest. The rest of this section will summarize the major lessons learned throughout the realization of this field report.

**Any static equipment slowly sinks in snow.** In the beginning of our deployment, we installed various static equipment to record position reference. A fixed GNSS reference receiver was installed to enable the RTK-GNSS and three *Trimble S7* robotic total stations were positioned to measure ground-truth robot poses in the *Garage* area, as shown in [Figure 18a](#) and [Figure 18b](#). Since the precision of these systems relies on the fact that the equipment remains static, we invested a considerable effort in shoveling and stabilizing snow in the areas where this equipment was installed to prevent the sinkage, see [Figure 18a](#). However, despite our efforts, we observed that the tripods carrying the equipment had sunk in the snow by several centimeters. The movement caused by this sinking effect made the affected ground-truth measurements unusable. The outside temperature oscillating around the water freezing point and the snow and rain precipitations shown in [Figure 9](#) led to snow melting, further increasing the tripod sinkage. Thus, significant effort and potentially using fixed structures is required to use such static equipment in winter conditions.

**Deep snow significantly affects UGV mobility.** As highlighted by Stansbury et al. (2004) and Lever et al. (2013), vehicle immobilization is a significant hazard when navigating on snow-covered terrain. We have attempted to manually drive the Warthog on a deep snow cover (i.e., 0.7 m), as shown in Figure 18c. During these runs, we noticed that robot mobility was significantly affected, especially during turning maneuvers. Also, the UGV chassis would float in sufficiently deep snow, resulting in reduced traction. At this point, turning maneuvers would make the robot sink even deeper, eventually requiring a human intervention to recover the robot. To prevent immobilization, backtracking maneuvers were necessary to compact the snow under the robot to maintain a minimal level of traction. This experience shows that immobilization prevention and recovery are required for mobile robot operation spanning multiple seasons in forest environments.



(a) Trimble S7 total stations. (b) Fixed Emlid GNSS antenna. (c) Deep snow navigation. (d) Run R7 battery breakdown.

Figure 18: Various lessons learned during this deployment (a): Total stations that were intended to measure the ground truth localization of the UGV in the *Garage* area. Despite considerable effort to prevent sinkage, those devices shifted significantly, resulting in unusable data. (b): The fixed GNSS antenna to enable RTK-GNSS. This device was placed in open areas to ensure good GNSS signal reception. (c): The Warthog UGV navigating in deep snow. A 1.8 m tall human operator stands next to the robot for scale. The snow level is estimated at 0.7 m in this area. The bottom of the robot chassis is resting directly on snow, affecting traction and eventually leading to UGV immobilization. (d): Warthog battery failure during run R7. A generator (in red) was used to recharge the robot batteries and later drive it manually back to the *Garage* POI.

**Winter weather significantly affected the battery capacity of the Warthog UGV.** Outside temperatures during this deployment reached a minimum of  $-15.5^{\circ}\text{C}$ , as shown in Figure 9. In our configuration, the Warthog is equipped with lead-acid batteries, whose capacity is known to be affected by low temperatures. Additionally, the CAMSO ATV T4S Tracks that the robot used to drive on snow-covered terrain significantly increased energy consumption compared to using wheels on solid ground. These factors contributed to a UGV battery depletion that occurred during run R7, as captured by the photo in Figure 18d. The robot recovery required a gas generator to charge the batteries, and the operators were required to drive back to the *Garage* POI in the middle of the night. Thus, assuming that the vehicle battery capacity is stable for a period spanning multiple seasons is false and will eventually lead to a system breakdown. Autonomous vehicle traversal planning should be conducted conservatively because the system recovery in remote environments is a costly operation.

**Resiliency to illumination variance is key to deploying mobile robots in northern environments.** Day length is subject to high variation in higher latitudes. To highlight this phenomenon, Figure 19 compares the sun radiation measured in the Montmorency forest during the deployment week and during the summer and winter solstice weeks. The days of the winter solstice week are short and receive minimum daylight. We argue that systems should be resilient to low or no-illumination conditions to enable year-long autonomy in the northern environments. In remote areas, no artificial light sources such as streetlights or buildings are present to provide illumination for the robot. As discussed by Congram and Barfoot (2021), vision-based localization is affected by low illumination conditions, even when using headlights. However, making robots resilient to navigate in dark environments is key to enable autonomy in the discussed environment. As highlighted by Krüsi et al. (2015), lidar-based localization is resilient to high illumination variations, whereas vision-based approaches may fail (Paton et al., 2017). This is due to the fact that lidars are active sensors that do not rely on an external energy source to produce measurements. Moreover, the lack of daylight has another practical impact. Deploying mobile robots in night conditions is difficult due to low visibility, low temperatures and fatigue, as can be seen in the system recovery snapshot shown in Figure 18d.



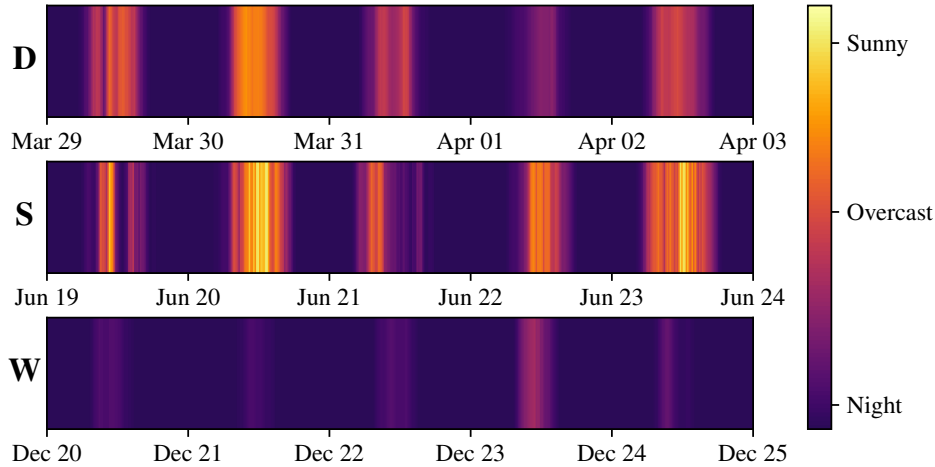


Figure 19: Sun radiation measured at the Montmorency forest for three distinct weeks. On top is the week during which this deployment (**D**) was taking place. In the middle is the week containing the 2021 summer (**S**) solstice. At the bottom is the week containing the 2020 winter (**W**) solstice. The coloring is proportional to the measured sun radiation every hour.

**Resilience to multi-seasonal change and unexpected events.** In a later deployment during the fall of 2021, we attempted to repeat all paths by using the maps shown in Figure 10 as reference. We successfully repeated paths A and C by localizing in a map that was recorded 209 days before. However, we had similar initialization problems as the ones discussed in Section 6.2 when attempting path B. After multiple trials, we managed to start a repeat run of B, but the robot became immobilized in a mud pit, as shown in Figure 20a. The repeat phase was cancelled at this point, and the robot was manually driven to the *Garage* POI. This experience supports our insight that immobilization prevention, recovery and dynamic map adjustment are key to enable multi-seasonal navigation. Later when attempting to repeat path C, we noticed that concrete blocks had been added to the path by the forest management, see Figure 20b. The robot was manually driven to avoid collision with these blocks and left to autonomously repeat the rest of the path. Once again, we argue that to deploy a robotic system in a boreal forest for a period spanning multiple years, autonomous navigation should be adaptive to the significant changes in the environment encountered during those deployments.



(a) The Warthog stuck in a mud pit.



(b) Previously unseen obstacles in path C.

Figure 20: Issues related to multi-season path repeating. (a): The Warthog stuck in a mud pit that was undetected during the teach phase of path B. Traversable terrain varies between seasons. (b): Obstacles that were moved in path C by human operators during summer. The presence of these obstacles required a human to take control of the UGV to avoid a collision.



## 7 Conclusion

This paper is a field report presenting over 18 km of autonomous path repeating in boreal forest trails and paths, including runs under harsh weather and high illumination variations. We have highlighted the impact of the boreal forest biome and winter conditions on autonomous navigation technologies. Based on the data recorded during these runs, we have shown that forest trails are GNSS-denied environments and that localization uncertainty is high in such trails due to low geometrical constraints in the vehicle's longitudinal direction. Moreover, we have highlighted the impact of snow accumulation and dynamic changes in the environment on lidar-based localization over multiple days in wintertime. We have discussed the requirement to improve the adaptiveness of autonomous navigation to enable multi-year robotic deployments in boreal forests.

While we have shown that our Weather-Invariant Lidar-based Navigation (WILN) system is able to autonomously repeat paths through a boreal forest in harsh winter conditions, more work remains to enable true long-term autonomy. Adaptive lidar-based localization to changes in the environment is key to allowing mobile robot deployment in boreal forests throughout an entire year. The ability to detect large variations in traction conditions will be key to preventing system failures from vehicle immobilization. Improving interaction between the localization and control systems would also be beneficial to the system adaptability. For example, modulating controller commands based on the localization uncertainty could prevent localization and mapping failures.

## Acknowledgments

This research was supported by the Natural Sciences and Engineering Research Council of Canada (NSERC) through the grant CRDPJ 527642-18 SNOW (Self-driving Navigation Optimized for Winter) and FORAC. Support from the Montmorency forest staff was crucial to allow safe UGV deployment in a closed environment. Meteorological data was a courtesy of the Hydrometeorology laboratory at Université Laval. Geographic data processing was provided by the Remote and Wood Sensing Laboratory of the University of New Brunswick.

## References

- Oliveira, L. F. P., Moreira, A. P., & Silva, M. F. (2021). Advances in forest robotics: A state-of-the-art survey. *Robotics*, 10(2).
- Marshall, J. A., Bonchis, A., Nebot, E., & Scheduling, S. (2016). Robotics in mining. In B. Siciliano & O. Khatib (Eds.), *Springer handbook of robotics* (pp. 1549–1576). Springer International Publishing.
- Kruijff, G. J. M., Janíček, M., Keshavdas, S., Larochelle, B., Zender, H., Smets, N. J. J. M., Mioch, T., Neerincx, M. A., Diggelen, J. V., Colas, F., Liu, M., Pomerleau, F., Siegwart, R., Hlaváč, V., Svoboda, T., Petříček, T., Reinstein, M., Zimmermann, K., Pirri, F., ... Sulk, M. (2014). Experience in system design for human-robot teaming in urban search and rescue. In K. Yoshida & S. Tadokoro (Eds.), *Field and service robotics: Results of the 8th international conference* (pp. 111–125). Springer Berlin Heidelberg.
- Simon, P. (2015). Military robotics: Latest trends and spatial grasp solutions. *International Journal of Advanced Research in Artificial Intelligence*, 4.
- Van Brummelen, J., O'Brien, M., Gruyer, D., & Najjaran, H. (2018). Autonomous vehicle perception: The technology of today and tomorrow. *Transportation Research Part C: Emerging Technologies*, 89(July 2017), 384–406.
- Russell, E., & Ritchie, J. C. (1988). Postglacial vegetation of Canada. *Bulletin of the Torrey Botanical Club*, 115, 231.
- Kubelka, V., Dandurand, P., Babin, P., Giguère, P., & Pomerleau, F. (2020). Radio propagation models for differential GNSS based on dense point clouds. *Journal of Field Robotics*, 37(8), 1347–1362.
- Paton, M., Pomerleau, F., MacTavish, K., Ostafew, C. J., & Barfoot, T. D. (2017). Expanding the Limits of Vision-based Localization for Long-term Route-following Autonomy. *Journal of Field Robotics*, 34(1), 98–122.
- Krüsi, P., Bücheler, B., Pomerleau, F., Schwesinger, U., Siegwart, R., & Furgale, P. (2015). Lighting-invariant Adaptive Route Following Using Iterative Closest Point Matching. *Journal of Field Robotics*, 32(4), 534–564.
- Lever, J. H., Delaney, A. J., Ray, L. E., Trautmann, E., Barna, L. A., & Burzynski, A. M. (2013). Autonomous GPR Surveys using the Polar Rover Yeti. *Journal of Field Robotics*, 30(2), 194–215.

- Apostolopoulos, D. S., Wagner, M. D., Shamah, B. N., Pedersen, L., Shillcutt, K., & Whittaker, W. L. (2000). Technology and Field Demonstration of Robotic Search for Antarctic Meteorites. *The International Journal of Robotics Research*, 19(11), 1015–1032.
- Moorehead, S., Simmons, R., Apostolopoulos, D. (.), & Whittaker, W. (L. Autonomous navigation field results of a planetary analog robot in antarctica. In: *Proceedings of international symposium on artificial intelligence, robotics and automation in space (isairas '99)*. 1999, June.
- Stansbury, R. S., Akers, E. L., Harmon, H. P., & Agah, A. (2004). Survivability, mobility, and functionality of a rover for radars in polar regions. *International Journal of Control, Automation and Systems*, 2(3), 343–353.
- Gifford, C. M., Akers, E. L., Stansbury, R. S., & Agah, A. (2009). Mobile Robots for Polar Remote Sensing. *The path to autonomous robots* (pp. 1–22). Springer US.
- Furgale, P., & Barfoot, T. D. (2010). Visual teach and repeat for long-range rover autonomy. *Journal of Field Robotics*, 27(5), 534–560.
- Churchill, W., & Newman, P. (2013). Experience-based navigation for long-term localisation. *The International Journal of Robotics Research*, 32(14), 1645–1661.
- Paton, M., MacTavish, K., Warren, M., & Barfoot, T. D. (2016). Bridging the appearance gap: Multi-experience localization for long-term visual teach and repeat. *2016 IEEE/RSJ International Conference on Intelligent Robots and Systems (IROS), 2016-Novem*, 1918–1925.
- Paton, M., MacTavish, K., Ostafew, C. J., & Barfoot, T. D. (2015). It's not easy seeing green: Lighting-resistant stereo Visual Teach & Repeat using color-constant images. *Proceedings - IEEE International Conference on Robotics and Automation, 2015-June*(6), 1519–1526.
- Clement, L., Kelly, J., & Barfoot, T. D. (2017). Robust Monocular Visual Teach and Repeat Aided by Local Ground Planarity and Color-constant Imagery. *Journal of Field Robotics*, 34(1), 74–97.
- McManus, C., Furgale, P., Stenning, B., & Barfoot, T. D. (2013). Lighting-invariant visual teach and repeat using appearance-based lidar. *Journal of Field Robotics*, 30(2), 254–287.
- MacTavish, K., Paton, M., & Barfoot, T. D. (2017). Visual triage: A bag-of-words experience selector for long-term visual route following. *2017 IEEE International Conference on Robotics and Automation (ICRA)*, 2065–2072.
- Paton, M., MacTavish, K., Berczi, L.-P., van Es, S. K., & Barfoot, T. D. (2018). I can see for miles and miles: An extended field test of visual teach and repeat 2.0. In M. Hutter & R. Siegwart (Eds.), *Field and service robotics* (pp. 415–431). Springer International Publishing.
- Clement, L., Gridseth, M., Tomasi, J., & Kelly, J. (2020). Learning Matchable Image Transformations for Long-Term Metric Visual Localization. *IEEE Robotics and Automation Letters*, 5(2), 1492–1499.
- Congram, B., & Barfoot, T. D. (2021). Relatively Lazy: Indoor-Outdoor Navigation Using Vision and GNSS. *2021 18th Conference on Robots and Vision (CRV)*, 25–32.
- Williams, S., & Howard, A. M. (2009). Developing monocular visual pose estimation for arctic environments. *Journal of Field Robotics*, 27(2), 145–157.
- Marshall, J., Barfoot, T., & Larsson, J. (2008). Autonomous underground tramming for center-articulated vehicles. *Journal of Field Robotics*, 25(6-7), 400–421.
- Sprunk, C., Tipaldi, G. D., Cherubini, A., & Burgard, W. (2013). Lidar-based teach-and-repeat of mobile robot trajectories. *IEEE International Conference on Intelligent Robots and Systems*, 3144–3149.
- Mazuran, M., Sprunk, C., Burgard, W., & Tipaldi, G. D. (2015). LexTOR: Lexicographic teach optimize and repeat based on user preferences. *Proceedings - IEEE International Conference on Robotics and Automation, 2015-June*(6), 2780–2786.
- Nieto, J., Guivant, J., Nebot, E., & Thrun, S. (2003). Real time data association for FastSLAM. *2003 IEEE International Conference on Robotics and Automation (Cat. No.03CH37422)*, 1(1), 412–418.
- Jagbrant, G., Underwood, J. P., Nieto, J., & Sukkarieh, S. (2015). Lidar based tree and platform localisation in almond orchards. In L. Mejias, P. Corke, & J. Roberts (Eds.), *Field and service robotics: Results of the 9th international conference* (pp. 469–483). Springer International Publishing.
- Zhang, J., & Singh, S. (2018). Laser-visual-inertial odometry and mapping with high robustness and low drift. *Journal of Field Robotics*, 35(8), 1242–1264.
- Ren, R., Fu, H., Xue, H., Li, X., Hu, X., & Wu, M. (2021). LiDAR-based robust localization for field autonomous vehicles in off-road environments. *Journal of Field Robotics*, (February), rob.22031.

- Babin, P., Dandurand, P., Kubelka, V., Giguère, P., & Pomerleau, F. (2019). Large-scale 3D mapping of subarctic forests. *Proceedings of the Conference on Field and Service Robotics (FSR)*. Springer Tracts in Advanced Robotics.
- Madgwick, S. O. H., Harrison, A. J. L., & Vaidyanathan, R. (2011). Estimation of IMU and MARG orientation using a gradient descent algorithm. *2011 IEEE International Conference on Rehabilitation Robotics*, 1–7.
- Bosse, M., & Zlot, R. (2009). Continuous 3D scan-matching with a spinning 2D laser. *2009 IEEE International Conference on Robotics and Automation*, 4312–4319.
- Pomerleau, F., Colas, F., & Siegwart, R. (2015). *A Review of Point Cloud Registration Algorithms for Mobile Robotics*. now Publishers Inc.
- Pomerleau, F., Magnenat, S., Colas, F., Ming Liu, & Siegwart, R. (2011). Tracking a depth camera: Parameter exploration for fast ICP. *2011 IEEE/RSJ International Conference on Intelligent Robots and Systems*, 3824–3829.
- Arya, S., & Mount, D. M. (1993). Approximate nearest neighbor queries in fixed dimensions. *Proceedings of the Fourth Annual ACM-SIAM Symposium on Discrete Algorithms*, 271–280.
- Pomerleau, F., Colas, F., Siegwart, R., & Magnenat, S. (2013). Comparing ICP variants on real-world data sets. *Autonomous Robots*, 34(3), 133–148.
- Pomerleau, F., Krusi, P., Colas, F., Furgale, P., & Siegwart, R. (2014). Long-term 3D map maintenance in dynamic environments. *2014 IEEE International Conference on Robotics and Automation (ICRA)*, (1), 3712–3719.
- Huskić, G., Buck, S., & Zell, A. (2017). A Simple and Efficient Path Following Algorithm for Wheeled Mobile Robots. *Advances in intelligent systems and computing* (pp. 375–387).
- Huskić, G., Buck, S., & Zell, A. (2019). GeRoNa: Generic Robot Navigation. *Journal of Intelligent & Robotic Systems*, 95(2), 419–442.
- Ministère des Forêts, de la Faune et des Parcs. (2017). *Ski de fond; Guide des principes d'aménagement, d'entretien et de signalisation des sentiers*. Collection de BAnQ, Québec, Canada. ISBN: 978-2-550-79935-1.
- Ministère des Forêts, de la Faune et des Parcs. (2021). *Guide d'application du règlement sur l'aménagement durable des forêts du domaine de l'état*. Gouvernement du Québec. Retrieved from <https://mffp.gouv.qc.ca/RADF/guide/annexes/annexe-4/>.
- World Meteorological Organization. (2019). Manual on codes. *World Meteorological Organization*. ISBN: 978-92-63-10306-2.
- Takasu, T., & Yasuda, A. (2009). Development of the low-cost RTK-GPS receiver with an open source program package RTKLIB. *International Symposium on GPS/GNSS*, (October), 4–6.
- Vaidis, M., Giguere, P., Pomerleau, F., & Kubelka, V. (2021). Accurate outdoor ground truth based on total stations. *Proceedings - 2021 18th Conference on Robots and Vision, CRV 2021*, 1–8.
- Mondoloni, S., Swierstra, S., & Paglione, M. (2005). Assessing Trajectory Prediction Performance & Metrics Definition. *24th Digital Avionics Systems Conference*, 1(April 2018).
- Baril, D., Grondin, V., Deschenes, S., Laconte, J., Vaidis, M., Kubelka, V., Gallant, A., Giguere, P., & Pomerleau, F. (2020). Evaluation of skid-steering kinematic models for subarctic environments. *2020 17th Conference on Computer and Robot Vision (CRV)*, 198–205.
- Gelfand, N., Ikemoto, L., Rusinkiewicz, S., & Levoy, M. (2003). Geometrically stable sampling for the ICP algorithm. *Fourth International Conference on 3-D Digital Imaging and Modeling, 2003. 3DIM 2003. Proceedings., 2003-Janua*, 260–267.
- Deschênes, S.-P., Baril, D., Kubelka, V., Giguère, P., & Pomerleau, F. (2021). Lidar scan registration robust to extreme motions. *2021 18th Conference on Robots and Vision (CRV)*, 17–24.